

Geophysical tests for habitability in ice-covered ocean worlds

Steven D. Vance¹, Mark P. Panning^{1*}, Simon Stähler^{2†}, Fabio Cammarano³, Bruce G. Bills¹, Sharon Kedar¹, Christophe Sotin¹, William T. Pike⁴, Ralph Lorenz⁵, Victor Tsai⁶, Hsin-Hua Huang^{6,7}, Jennifer M. Jackson⁶, Bruce Banerdt¹

¹Jet Propulsion Laboratory, California Institute of Technology, Pasadena, California, USA

²Dept. of Earth and Environmental Sciences, Ludwig-Maximilians-Universität, Munich, Germany

³Dipartimento di Scienze Geologiche, Università Roma Tre, Largo S. L. Murialdo 1, 00146 Rome, Italy

⁴Department of Electrical and Electronic Engineering, Imperial College, London, United Kingdom

⁵Johns Hopkins University Applied Physics Laboratory, Laurel, USA

⁶Seismological Laboratory, California Institute of Technology, Pasadena, California, USA

⁷Institute of Earth Sciences, Academia Sinica, Taiwan

arXiv:1705.03999v1 [astro-ph.EP] 11 May 2017

*now at Jet Propulsion Laboratory, California Institute of Technology, Pasadena, California, USA

†now at Institute of Geophysics, ETH Zürich, Zürich, Switzerland

Abstract

Geophysical measurements can reveal the structure of icy ocean worlds and cycling of volatiles. The associated density, temperature, sound speed, and electrical conductivity of such worlds thus characterizes their habitability. To explore the variability and correlation of these parameters, and to provide tools for planning and data analyses, we develop 1-D calculations of internal structure, which use available constraints on the thermodynamics of aqueous MgSO_4 , NaCl (as seawater), and NH_3 , water ices, and silicate content. Limits in available thermodynamic data narrow the parameter space that can be explored: insufficient coverage in pressure, temperature, and composition for end-member salinities of MgSO_4 and NaCl , and for relevant water ices; and a dearth of suitable data for aqueous mixtures of $\text{Na-Mg-Cl-SO}_4\text{-NH}_3$. For Europa, ocean compositions that are oxidized and dominated by MgSO_4 , vs reduced (NaCl), illustrate these gaps, but also show the potential for diagnostic and measurable combinations of geophysical parameters. The low-density rocky core of Enceladus may comprise hydrated minerals, or anhydrous minerals with high porosity comparable to Earth's upper mantle. Titan's ocean must be dense, but not necessarily saline, as previously noted, and may have little or no high-pressure ice at its base. Ganymede's silicious interior is deepest among all known ocean worlds, and may contain multiple phases of high-pressure ice, which will become buoyant if the ocean is sufficiently salty. Callisto's likely near-eutectic ocean cannot be adequately modeled using available data. Callisto may also lack high-pressure ices, but this cannot be confirmed due to uncertainty in its moment of inertia.

Key Points:

- Provides tools for planning and data analysis needed for geophysical investigations of icy ocean worlds
- Constrains interior structures and explores the influence of composition using self-consistent thermodynamics of ices, oceans, and silicates
- Demonstrates the potential for obtaining a combination of geophysical signatures that are diagnostic of conditions that might support life

1 Introduction

Geophysical measurements can reveal the interior properties of icy ocean worlds. Such measurements can point to the presence and temporal variability of fluids and gases, thus identifying potential habitable niches for life. The thickness of ices and depth of the ocean determine the conditions under which life might exist. Similarly, the global fluxes of chemical energy must be understood in terms of a world's interior structure and evolution, which can only be illuminated by geophysical means. Earth's biogeochemical cycles rely on the mantle for a continuous supply of reduced materials [e.g., *Hayes and Waldbauer, 2006*] balanced by a continuous supply of oxidants [e.g., *Catling and Claire, 2005*].

Consider the example of Jupiter's moon, Europa. The small value of Europa's gravitational moment of inertia inferred from *Galileo* flybys [Table 1; *Anderson et al., 1998; Schubert et al., 2004*] suggests a differentiated body consistent with strong tidal heating expected to have occurred throughout its history [*O'Brien et al., 2002; Sotin et al., 2009*]. It is commonly assumed that Europa's ocean started out hot and reducing, and after some time (~ 2 Gyr) may have oxidized due the flux of radiolytic materials produced at the surface [*Pasek and Greenberg, 2012*]. The flux today of reduced hydrogen and other materials from high-temperature hydrothermal activity and water-rock alteration has been estimated at $> 10^9$ moles yr^{-1} , with potentially an order of magnitude greater oxidizing flux from materials produced at the surface [*Hand et al., 2007; Vance et al., 2016a*].

The example of Europa, analogous to its smaller sibling Enceladus, illustrates how the accumulated effects of an ocean world's redox evolution can be measured by geophysical means. Whether Europa had its own paleozoic (or azoic) "great oxidation event" [*Lyons et al., 2014*] depends on its initial composition and geodynamic evolution. The ocean's pH and associated salinity are the integrated results of a world's geochemical evolution; a low pH ocean would be dominated by sulfate anions, whereas a neutral or basic ocean would be dominated by chlorides [*Zolotov, 2008; Zolotov and Kargel, 2009*].

Ocean composition measurements cannot be based on surface imaging or atmospheric sampling alone, due to unknown fractionation within the ice. Chlorides inferred from surface infrared reflectance spectra of Europa's surface [*Brown and Hand, 2013; Fischer et al., 2015; Ligier et al., 2016*] are not a conclusive proxy for seawater salinity, because chlorides fractionate into freezing sea ice relative to sulfates [*Gjessing et al., 1993; Maus et al., 2011*]. Di-

rect measurement of an ocean's salinity and characterization of the ice can only be achieved in the near term by geophysical means.

The habitability of larger icy ocean worlds may also be probed with geophysical measurements. In Ganymede, Callisto, and Titan, high-pressure ices have been regarded as limiting water-rock interactions that regulate redox and ocean composition, and which are thereby critical for supporting life. However, convective transport within high-pressure ices should proceed near the solidus temperature, leading to substantial melt at the ice-rock interface, and within the upper part of the ice [Choblet *et al.*, 2017]. Briny fluids under pressure can have densities exceeding those of high pressure ices, and may occupy the interface between rock and ice [Hogenboom *et al.*, 1995; Vance *et al.*, 2014]. Dissolved ions can incorporate into high-pressure ice VI (and possibly phases II, III, and V) to a much greater extent than in ice Ih, potentially decreasing the density of the ices and enhancing near-solidus convection [Journaux *et al.*, 2017].

Seismic investigations could characterize habitability of ocean worlds [Vance *et al.*, 2016b] in a manner that is highly complementary to other measurements on missions exploring the habitability of ocean worlds, particularly those of NASA's planned Europa Mission [Pappalardo *et al.*, 2016] and ESA's JUICE mission [Grasset *et al.*, 2013]: Radar investigations will examine the density, temperature, and composition of the ices covering Europa, Ganymede, and Callisto. The RIME and REASON instruments will reveal the upper km of the ice with a range resolution as small as 15 meters, and will sound to as much as 45 km in cold ice with a range resolution as small as 30 m [Grima *et al.*, 2015]. Whereas radio waves are sensitive mainly to density, electrical conductivity, and crystal orientation fabric (COF), seismic waves are influenced mainly by density, COF, and temperature [Diez, 2013]. Prior radar information thus provides a powerful constraint for extracting more detailed information from the deeper interior. Similar combined investigations of Antarctic glaciers have revealed sub-ice lake and low-velocity layers at the water-rock interface consistent with a sedimentary layer [Bell *et al.*, 1998]. Electromagnetic measurements (ICEMAG and PIMS) on the planned Europa Clipper mission [Pappalardo *et al.*, 2016] will use Europa's induced response to Jupiter to constrain the ocean's depth and electrical conductivity. Seismology could directly measure the ice and ocean thicknesses, and could leverage constraints on electrical conductivity to narrow the range of plausible models for ocean salinity. Seismology provides comparable or better vertical resolution, and a measure of the magnitude and nature of ongoing activity. Seismic measurements might also probe below the ice-ocean interface

to reveal the deeper interior, with the potential to constrain the current thermal state of the rocky interior [Cammarano *et al.*, 2006]. This combination of seismology with other methods may be deployed at other ocean worlds to reveal the nature of a potential habitat in the ice, ocean, seafloor, and below.

Forward models of the interiors of icy ocean worlds are needed in order to plan future mission designs and measurements of their interior dynamics and habitability. Here, we develop global one-dimensional models to assess how combined seismic, gravity, and magnetic measurements may be used to investigate the habitability of ocean worlds. We use the models to consider how the ocean's composition might influence the configuration and thickness of ice layers. Another important function of this work is to test the limits of available data describing material properties.

In Section 2, we describe the workings of the model and limitations of available data. In Section 3, we describe applications to confirmed ocean worlds, Ganymede, Europa, Enceladus, Titan, and Callisto. In Sections 4 and 5 we discuss possible tests for habitability, and thermodynamic measurements needed for further modeling.

2 Materials and Methods

We assess interior density, elastic and anelastic structure, and associated seismic sources and signatures, building on prior work that focused only on Europa [Cammarano *et al.*, 2006]. Added to this is an investigation of the electrical conductivity of fluids based on available measurements.

The interior structure model propagates density and temperature profiles downward from the ice I layer from boundary conditions of the surface and ice-ocean boundary temperature, as per Vance *et al.* [2014, ; Appendix A:]. Significant improvements have been made for speed, modularity to enable future work, and added geodynamics and geochemistry for the ice I layer and deeper interior. Depths of transition between compositional layers {ice, ocean, (ice), rock, (iron)} are computed from bulk density and gravitational moment of inertia (C/MR^2 ; Table 1). Solid state convection in the ice I layer has been added, and is included by iteration after the initial model run. Gravitational acceleration increases with depth in the relatively low density ice and liquid layers approaching the solid core [by up to 25% in the case of Ganymede; Vance *et al.*, 2014], so depth-dependent gravity is computed after the initial computation of the pressure-dependent adiabatic gradient. Slowly rotating body Cal-

listo may not be in hydrostatic equilibrium [Gao and Stevenson, 2013] and so the moment of inertia inferred from simultaneous measurements of J_2 and C_{22} may be overestimated by as much as 10%. We consider this effect in the Section 3.

Table 1. Properties of ocean worlds

	Radius (km)	Density (kg m ⁻³)	Moment of Inertia
Europa ^a	1565.0±8.0	2989±46	0.346±0.005
Ganymede ^a	2631±1.7	1942.0±4.8	0.3115±0.0028
Callisto ^a	2410.3±1.5	1834.4±3.4	0.3549±0.0042
Enceladus ^{b,c}	252.1±0.2	1609±5	0.335
Titan ^c	2574.73±0.09	1879.8±0.004	0.3438±0.0005

^aSchubert et al. [2004], ^bThomas [2010]; Iess et al. [2014], ^cJacobson et al. [2006]; Iess et al. [2012]

2.1 Thermodynamics and Geodynamics

The model’s current modules are described in the following subsections. Thermodynamic modules provide self-consistent density, thermal expansivity, specific heat capacity, and sound speed constrained by available data, using published methodologies to easily and rapidly retrieve values. Adding new equations of state for alternate ocean compositions or updated material properties is straightforward.

2.1.1 Ices

The thermodynamic properties of water ice phases Ih, II, III, V, and VI are taken primarily from Choukroun and Grasset [2010], which fit available measurements of heat capacity, enthalpy, and specific volume over the broad range of pressure and temperature occurring in icy worlds. Corresponding bulk sound speeds (v_C) ($(\partial\rho/\partial P)_T = v_C^{-2} + \alpha^2 T/C_P$) have very large pressure derivatives and misfit available measurements by up to 100% (right-hand pane in Figure 1). To provide sound speeds consistent with available measurements and mostly consistent with thermodynamic data, compressional and transverse sound speeds in these phases are matched to sound speeds from bulk adiabatic Brillouin measurements in polycrystalline ice at -35.5°C to 1 GPa [Gagnon et al., 1988, 1990] to within their assigned errors. Adiabatic shear and bulk moduli (μ , K_S) and their pressure derivatives were adjusted from

Shaw [1986] to fit compiled sound speeds from *Gagnon et al.* [1990] to better than 1.5%.

Sound speeds (Figure 2) are computed as

$$V_S = \left[\frac{\mu}{\rho} \right]^{1/2} \quad (1)$$

$$V_P = \left[\frac{K_S}{\rho} + \frac{4}{3} V_S^2 \right]^{1/2} \quad (2)$$

This strategy does not reproduce the negative slope of sound speed with temperature of $\approx -2 \text{ m s}^{-1} \text{ K}^{-1}$ [*Vogt et al.*, 2008]. Further measurements of sound velocities in ices would aid both seismic data analysis and geodynamics.

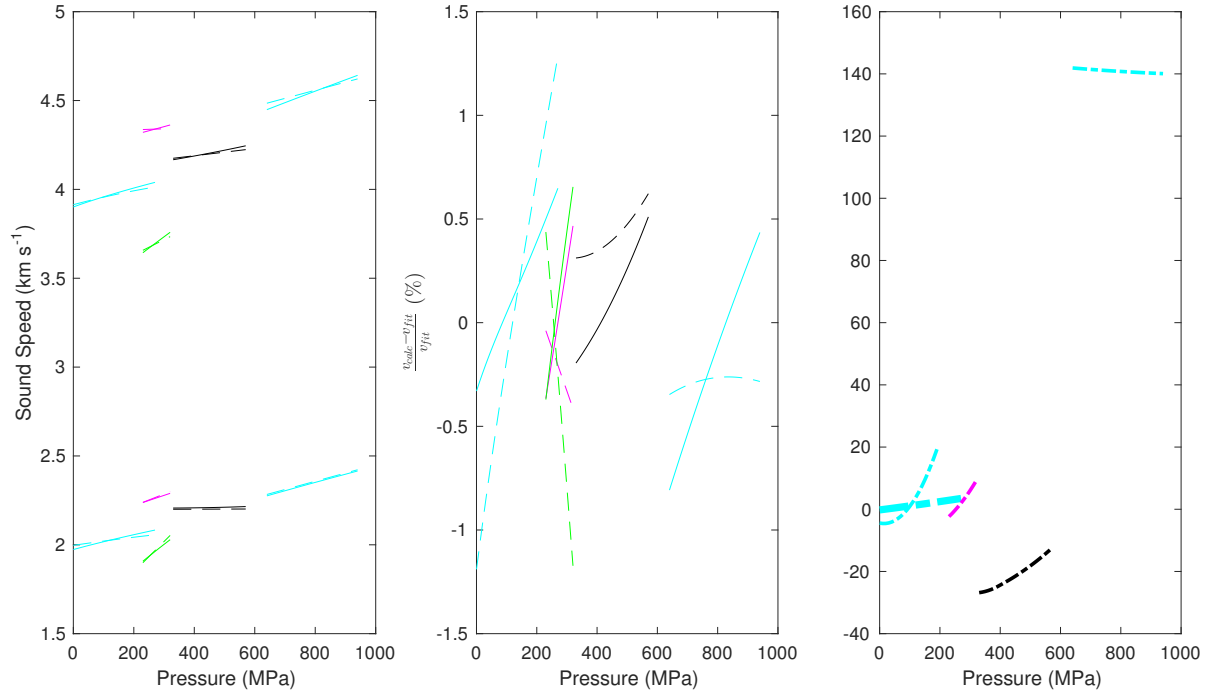


Figure 1. Evaluation of sound speeds near 240 K. Sound speeds (left) from [*Gagnon et al.*, 1988] and [*Gagnon et al.*, 1990] (—) compared with the fit used in this work. Middle: deviations (%) between published and fit values (V_P —, V_S --). Right: Misfit (%) between bulk sound speeds computed from published values and compiled thermodynamics [*Choukroun and Grasset*, 2010].

Table 2. Bulk and Shear Moduli for Ices

Crystalline Phase	K_S^a GPa	$K_S'^b$	K_S'' GPa ⁻¹	μ GPa	μ'^b	μ'' GPa ⁻¹
I _h ^c	9.5	0.33	-0.026	3.3	0.537	-0.025
II	13.89	1.6	—	5.15	3.5	—
III	8.9	3.65	—	2.7	6.55	—
V	11.8	4.8	—	5.7	0.9	—
VI	14.6	4.1	—	5.0	3.0	—

^aAdapted from *Gagnon et al.* [1990], ^bFit from *Shaw* [1986], ^c*Gagnon et al.* [1988]

2.1.2 Fluids

We examine the influence of ocean salinity in each ocean world by comparing compositions of pure water and 10 wt% (~1 molal) MgSO₄. Seawater compositions are examined for Europa and Enceladus. Solutions containing 3 wt% NH₃ are considered for Titan.

The thermodynamic module for the fluids (fluidEOS) provides properties for aqueous magnesium sulfate from *Vance and Brown* [2013]. Properties are retrieved by three-dimensional spline interpolation, with extrapolation above 0.8 GPa and 2.5 mol kg⁻¹. The melting point depression is computed using the Margules parameterization for the activity of water for MgSO₄ *Vance et al.* [2014] and NH₃ *Choukroun and Grasset* [2010]. Contours of sound speed for water and 10 wt% MgSO₄ are shown in Figure 2. The Gibbs Seawater package [GSW; *McDougall and Barker*, 2011] provides self-consistent thermodynamics for seawater reliably to 100 MPa, with reasonable stability for standard concentration to the 210 MPa limitation of its equation of state for ice I_h. Thermodynamics of aqueous ammonia are from [*Tillner-Roth and Friend*, 1998] with phase equilibria from .

The electrical conductivity of 0.01 mol kg⁻¹_{H₂O} (molal) magnesium sulfate (aq) is computed along geotherms based on measurements at 298 K and 323 K, and pressures up to 784.6 MPa [*Larionov and Kryukov*, 1984]. Extrapolation to 273 K is applied with a scaling factor of 0.525 as per *Hand and Chyba* [2007], with linear interpolation and extrapolation to 250 K and 1.6 GPa. Figure 3 shows the variation of electrical conductivity with pressure, temperature, and concentration in the main region down to 273 K. Conductivity depends strongly on concentration, but direct measurements at elevated pressure are unavailable.

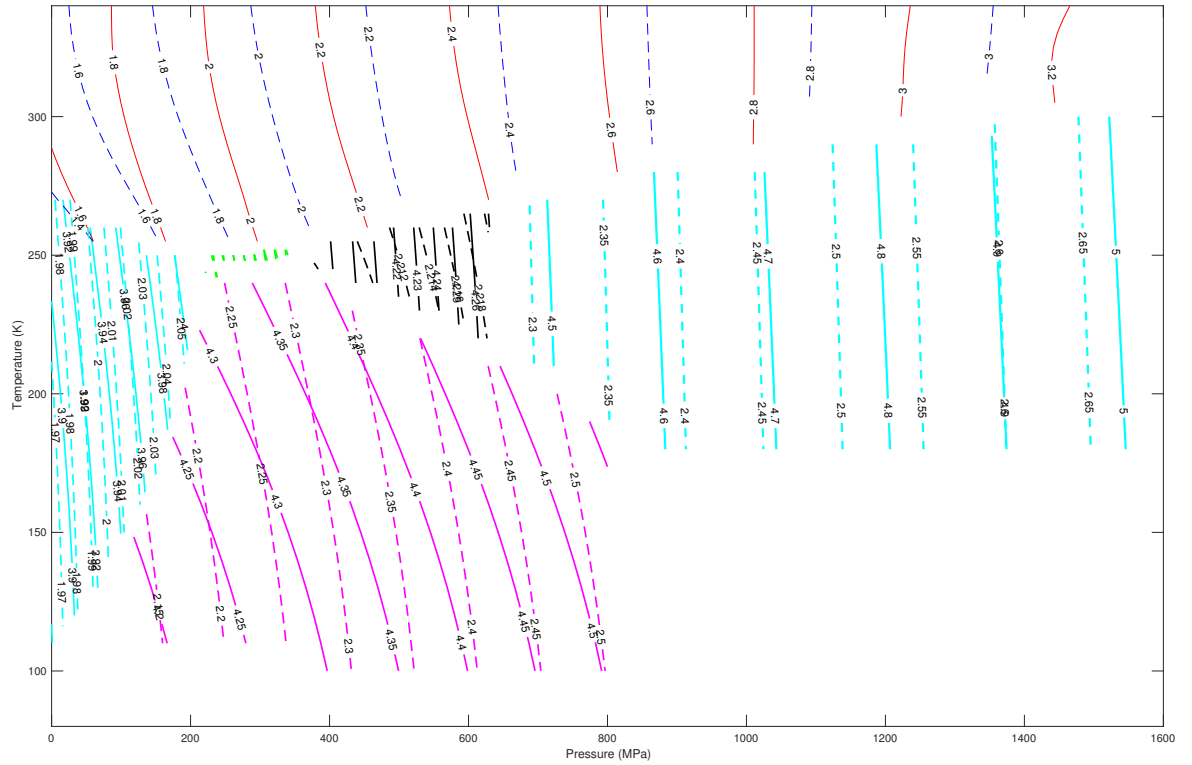


Figure 2. Contours of sound speed versus pressure (MPa) and temperature (K). In the ice stability field ($T \sim < 260$ K): v_P (—) and v_S (---). In the fluid stability range: v_P in 10 wt% MgSO_4 (—) and pure water (---). Fluid-liquid phase boundaries are for the 10 wt% case.

Measurements taken at standard pressure show a factor of 40 increase for magnesium sulfate up to 1 molal [Hand and Chyba, 2007, Figure 1]. This linear scaling with concentration is used in our calculations. GSW includes electrical conductivity.

2.1.3 Rock

We model the silicate portions of planetary bodies using available thermodynamic software. Stable mineralogies, densities, and seismic velocities of the bulk rock are determined from the profiles of present-day temperature (T), composition (C), and pressure (P) for a range of possible compositions using PERPLEX 6.7.3 [Connolly, 2005, 2009; PERPLEX]. The program solves the Gibbs energy minimization based on specified thermodynamic databases and thermoelastic properties for end-member mineralogical phases. Av-

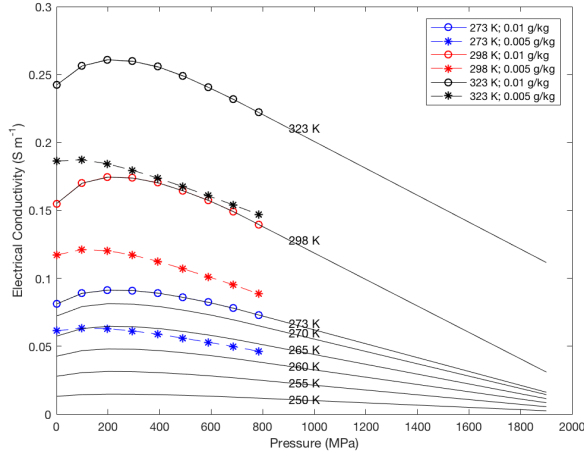


Figure 3. Electrical conductivity of 0.005 molal and 0.01 molal MgSO_4 from *Larionov and Kryukov* [1984]. Contours show linear extrapolation above 800 MPa and below 273 K for 1 molal conductivity.

erage properties of the bulk rock are determined through classical Voigt-Reuss-Hill averaging scheme. High-pressure (>5GPa) polythermal equations of state (Murnaghan, Birch-Murnaghan) were stabilized by computing the temperature derivative of the bulk modulus as a function of the pressure derivative of the bulk modulus and the expansivity at the reference pressure, as per *Helfrich and Connolly* [2009].

2.1.4 Bulk Mineralogy

Following previous work for Europa by *Cammarano et al.* [2006], we consider two different dry compositions: an Earth-like pyrolite composition and L-LL chondritic model (Table 3). We also consider updated compositions that include sodium, as per *Cammarano et al.* [2011]. The computations use the formalism and thermoelastic properties dataset of *Stixrude and Lithgow-Bertelloni* [2011], which accounts for six main oxides: SiO_2 , MgO , FeO , CaO , Al_2O_3 , Na_2O . The database was assembled with a focus on using available elastic moduli of Earth's mantle minerals extending to pressures in the 100 GPa range. Variations in major oxides, especially in iron content, have the largest effect on density. The range of densities within the plausible range of pressure-temperature conditions covering all icy moons is small compared with Earth's mantle. Densities for both pyrolite and L-LL chondrite composition exceed 3000 kg m^{-3} . This is also true for larger variations in density arising from changes in oxide composition.

2.1.5 Hydrous Minerals

The effects of hydrous compositions are also considered, using the database of *Holland and Powell* [2011], which includes more mineral species while retaining thermodynamic self-consistency. We use the same compositions described in the previous section, but at partially hydrated or water-saturated conditions. Serpentinization may be important as a source of H₂ for life [e.g., *Müntener*, 2010; *Vance et al.*, 2016a], but it may not reduce the density of the rocky siliceous parts of icy worlds because hydrated silicates are not thermodynamically stable at low pressures, and at temperatures higher than 900 K [e.g., *Ulmer and Trommsdorff*, 1995].

2.1.6 Porosity

Because of the low confining pressures occurring in smaller icy ocean worlds, porosity becomes important at much greater depths than on Earth. Tidal forcing and thermal fracturing may aid in developing a porous interior, as putatively found at Enceladus [*Vance et al.*, 2007]. In general, porosity decreases with increasing lithostatic pressure, which closes pore spaces, cracks and fractures. *Vitovtova et al.* [2014], for example, estimated Earth's mantle porosity at a few percent at a depth of 10 km, decreasing to 0.01-0.1% at 35 km. However the trend can be more complex. For example an increase in porosity with depth is recorded for the borehole of the Kola peninsula, the deepest on Earth, at 12 km [*Kozlovsky*, 1987].

Direct and indirect measurements suggest the porosity of Earth's oceanic and continental crust is large, especially in the uppermost part [ranging from 5 to 10%, e.g. *Carlson*, 2014]. For example, high V_P/V_S at 25-45 km depth suggest a porosity around 2.7-4.0% [*Peacock et al.*, 2011], associated with the presence of fluid saturated zones. Alternatively, crack anisotropy may partially explain the high V_P/V_S [*Wang et al.*, 2012]. Experimental studies find that voids are closed at pressures higher than 0.25 GPa [*Kern*, 1990] unless fluids fill the voids. Recent laboratory experiments in a porous natural sample of crustal rock [i.e., *Saito et al.*, 2016] indicate that porosity closure is active up to ~0.6 GPa. In spite of low remanent porosity, the effect on seismic velocities is a few percent, and thus should be accounted for. The V_P/V_S ratio, in this case, decreases in the pore spaces not filled by fluids. In crystalline rocks, the intergranular porosity is usually small, but may increase due to water-rock interactions [e.g., *Tutolo et al.*, 2016].

We model the decrease of porosity with pressure using the empirical formula provided by *Vitovtova et al.* [2014]: $\log(\phi) = -0.65 - 0.1d + 0.0019d^2$, where ϕ is the total porosity (assumed to be equal to the effective one) and d the depth in km. We convert depth to pressure using the pressure profile from the preliminary reference earth model [PREM; *Dziewonski and Anderson, 1981*]. The reduction in density due to porosity is obtained from $\rho = \phi\rho_f + (1 - \phi)\rho_g$, where the rock density ρ_g is the obtained density from thermodynamic modeling. The pore spaces are assumed to be filled by water (*i.e.*, $\rho_f = 1023 \text{ kg m}^{-3}$).

Concerning the effects of porosity on seismic velocities, few experiments exist on the effects of low porosity crystalline rocks. [e.g., *Todd and Simmons, 1972; Christensen, 1989; Darot and Reuschlé, 2000; Yu et al., 2016*]. In general, the effect of pore pressure on seismic velocities is inverse to that of the confining pressure; seismic velocities are expected to decrease as pore pressures increase. The expected behavior is complicated by the shape, distribution and connectivity of pores, and the presence of cracks and fractures. We account for the decrease in V_P as a function of porosity using the relation suggested by *Wyllie et al.* [1958]. The decrease in V_S should be greater; *Christensen* [1989] found a decrease of 9% and 26% for V_P and V_S , respectively, when increasing pore pressure from atmospheric pressure to 85% in a very porous (3.9%) lherzolite xenolith at 150 MPa of confining pressure. We scale the decrease in V_S to be 2 times larger in percentage than V_P . Although approximate, these corrections account for the expected qualitative effects of water-filled porous spaces on seismic velocities.

For models specifying an iron core, the starting density of the rock is adjusted to match the average predicted by the model.

2.1.7 Iron Core

When including an iron core, we assume the γ (face-centered-cubic) or molten FeS mineralogies described by *Cammarano et al.* [2006] (Table 4). The density of the solid core for $X_{FeS} < 5\%$ is

$$\rho_{core} = \frac{\rho_{Fe}\rho_{FeS}}{X_{FeS}(\rho_{Fe} - \rho_{FeS}) + \rho_{Fe}} \quad (3)$$

The choice of core composition does not affect the results for the properties of the deep ocean, which is the main focus of this paper.

Table 3. Chemical compositions (in mol%) considered for the rocky component

	Pyrolite ^a	L-LL Chondrite ^b	Pyrolite ^b	L-LL Chondrite ^b
SiO ₂	38.71	38.73	38.66	42.78
MgO	49.85	38.73	48.53	39.68
FeO	6.17	14.98	5.72	13.98
CaO	2.94	2.12	3.50	2.13
Al ₂ O ₃	2.22	1.36	3.59	1.43
Na ₂ O	0.11	1.02	–	–

^aCammarano *et al.* [2011];^bmodified from Cammarano *et al.* [2006]

Table 4. Iron and Iron-Sulfur properties.

	fcc- γ -Iron ^a	Fe-S (5% < X_{FeS} < 20%) ^b
ρ	8000	5150-(%S-10)×50
α , 10 ⁻⁵ K ⁻¹	5	9.2
K_S , GPa	156	53.2-(%S-10)×2
$\partial K_S/\partial P$	5.0	4.66
$\partial K_S/\partial T$, Pa K ⁻¹	-0.040	–
G , GPa	76.5	–
$\partial G/\partial P$	2	–
$\partial G/\partial T$, Pa K ⁻¹	-0.023	–

^aCammarano *et al.* [2006];^bSanloup *et al.* [2000]

2.2 Anelasticity (Seismic Attenuation)

Frequency dependent seismic attenuation is computed as [Cammarano *et al.*, 2006]

$$\frac{Q_S}{\omega^\gamma} = B_a \exp\left(\frac{\gamma H(P)}{RT}\right), H(P) = g_a T_m \quad (4)$$

in which $B_a = 0.56$ is a normalization factor, ω is the seismic frequency, exponent $\gamma = 0.2$ is the frequency dependence of attenuation. H , the activation enthalpy, scales with the melting temperature T_m with the anisotropy coefficient g_a . Chosen values of g_a for ices {I,II,III,V,VI} are {22, 30, 25, 27, 28, 30}. For the rocky mantle we assume $g_a=30$. Atten-

uation in Earth’s ocean is small ($Q > 10^4$), and is ignored. If a metallic core is present, its value of Q_S/ω^γ is set to 10^4 .

3 Results

For each ocean world, we display the bulk interior structure, and detailed ocean and ice structure for adiabatic profiles spanning the range of heat flux values consistent with the inferred existence of an ocean.

3.1 Ganymede

The structure for Ganymede is nearly identical to those discussed by *Vance et al.* [2014], but with the addition of solid state convection in the ice I layer. Figure 4 shows the configuration of density as a function of pressure, and corresponding temperature, sound speed, and electrical conductivity versus inferred depth for oceans with 0 and 10 wt% MgSO_4 . For the chosen ocean salinity and core composition (Table 5), the silicate layer depth exceeds 800 km. Buoyant ice III occurs at the base of the ocean for the coldest adiabat. For the warmest adiabat, ice VI is also buoyant and ice V is absent.

Heat flux spans a range from 15 to 25 mW^{-2} , consistent with model-based constraints on Ganymede’s thermal-orbital history [e.g., *Bland et al.*, 2009]. Higher heat fluxes, and ice as thin as ~ 10 km are still in accord with the formation of grooved terrains on the surface [*Hammond and Barr*, 2014]. However these would require tidal heating. At present, such heating is probably negligible [e.g., *Bland and McKinnon*, 2015], but residual heat may also lead to unexpectedly thinner ice than considered here. Solid state convection is nearly four times more efficient than conductive cooling for the coldest adiabat.

The convecting ocean shows temperature increasing strongly with depth due to the high compressibility of the fluids at 100 MPa relative to the solids. The addition of MgSO_4 decreases the compressibility and steepens the adiabat. Sound speeds are distinct for the different ice phases, and also for the freshwater and saline oceans. Sound speeds increase with depth everywhere.

The temperature dependence of electrical conductivity distinguishes among the different profiles. The two warmest adiabats extend to sufficiently high pressure that the pressure derivative of electrical conductivity changes from increasing to decreasing. This is in accord

with recent predictions investigations of water's interaction with dissolved ions at high pressures [Vance *et al.*, 2015; Schmidt and Manning, 2017].

Figure 5 shows the global structure: P- and S- wave speeds, pressure temperature and density, and anelasticity. The best fit mineral structure is a chondrite with 1wt% hydration; Table 3). The presence of a liquid core is well documented for Ganymede [Kivelson *et al.*, 2002]. We specify a 20 wt% FeS core composition.

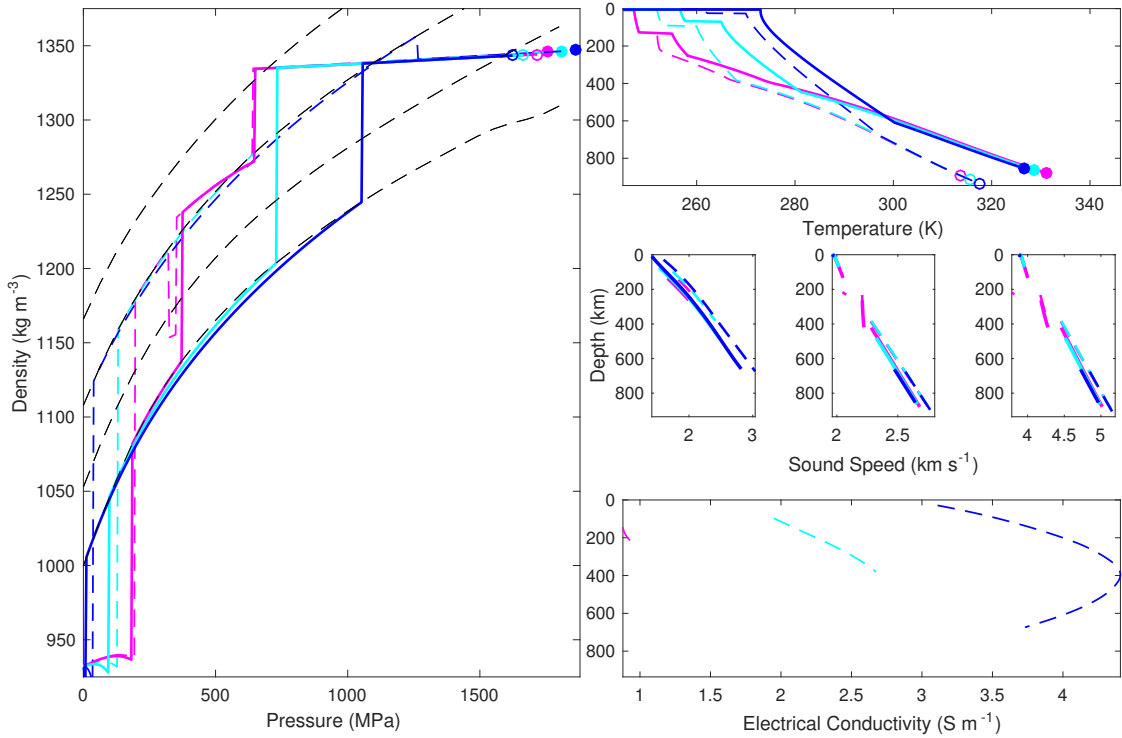


Figure 4. Ganymede: Oceans with 10 wt% MgSO₄(aq) (—), pure water (---) for T_b as in Table 5. Left: Density versus pressure. Reference fluid densities along the melting curve for MgSO₄ for {0,5,10,15} wt% increase with increasing concentration. Right: Corresponding depth-dependent temperature (top), sound speed in the fluids and ices (fluid, V_S , V_P middle left to right), and electrical conductivity (bottom). Circles indicate the transition to the silicate interior.

3.2 Europa

Models for Europa (Figs. 6 and 12) are adjusted through the choice of T_b to compare ice thicknesses of 5 and 30 km. Model europas have seafloor depths slightly in excess of 100 km, consistent with the choice of silicate density and the assumption of a metallic core.

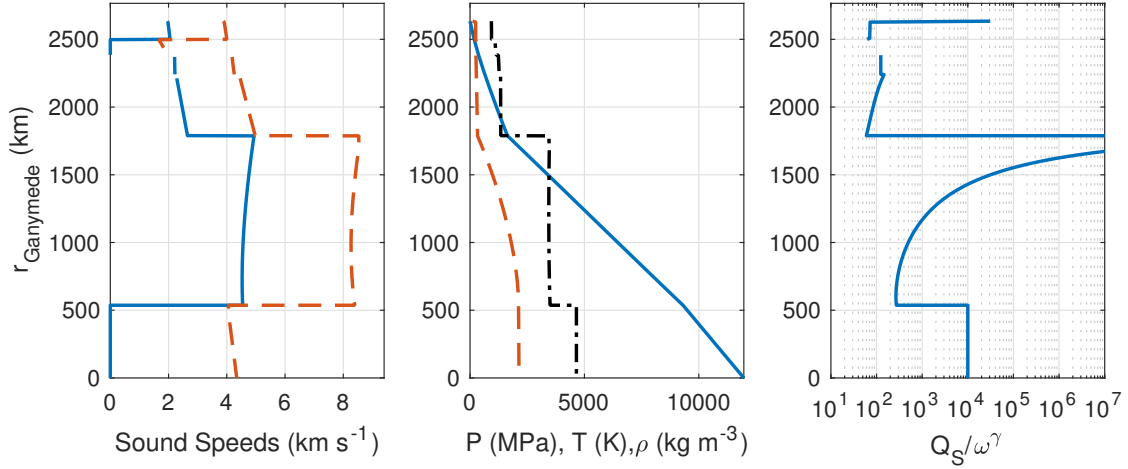


Figure 5. Ganymede: global interior structure for an ocean with 10 wt% $\text{MgSO}_4(\text{aq})$ and ice Ih thickness of 134 km. Left: V_S (—) and V_P (---). Middle: Temperature (—) and density (---). Right: Anelasticity.

For identical ice thicknesses, seawater salinity suppresses the melting of ice more strongly than MgSO_4 . Sound speeds for seawater are comparable to those of water, whereas MgSO_4 sound speeds are larger by more than 10%. Oceans with MgSO_4 have higher electrical conductivity due to both higher ionic strength and higher temperature. Reference density profiles along the melting curve for seawater are unstable above 80 MPa for concentrations twice that of seawater ($2S_0$).

Sound speeds are low in the hydrous upper portion of the rocky interior, increasing with depth due to dehydration. The Na_2O -bearing pyrolite with 1 wt% hydration provides an average rock density closest to the input value of 3300 kg m^{-3} . We specify a core composition of pure iron.

3.3 Enceladus

Models for Enceladus (Figs. 8) are adjusted through the choice of T_b to compare ice thicknesses of 10 and 50 km corresponding to constraints at the south polar plume and in the rest of the global ocean, respectively [McKinnon, 2015; Beuthe, 2016; Thomas et al., 2016]. MgSO_4 is considered, despite strong inferences that the ocean has a high pH and thus is dominated by chlorides [Postberg et al., 2011; Glein et al., 2015]. As with Europa, the different ocean compositions have distinct profiles in temperature, density, electrical conductivity, and sound speed. For models examining a 10-km-thick ice Ih layer potentially present

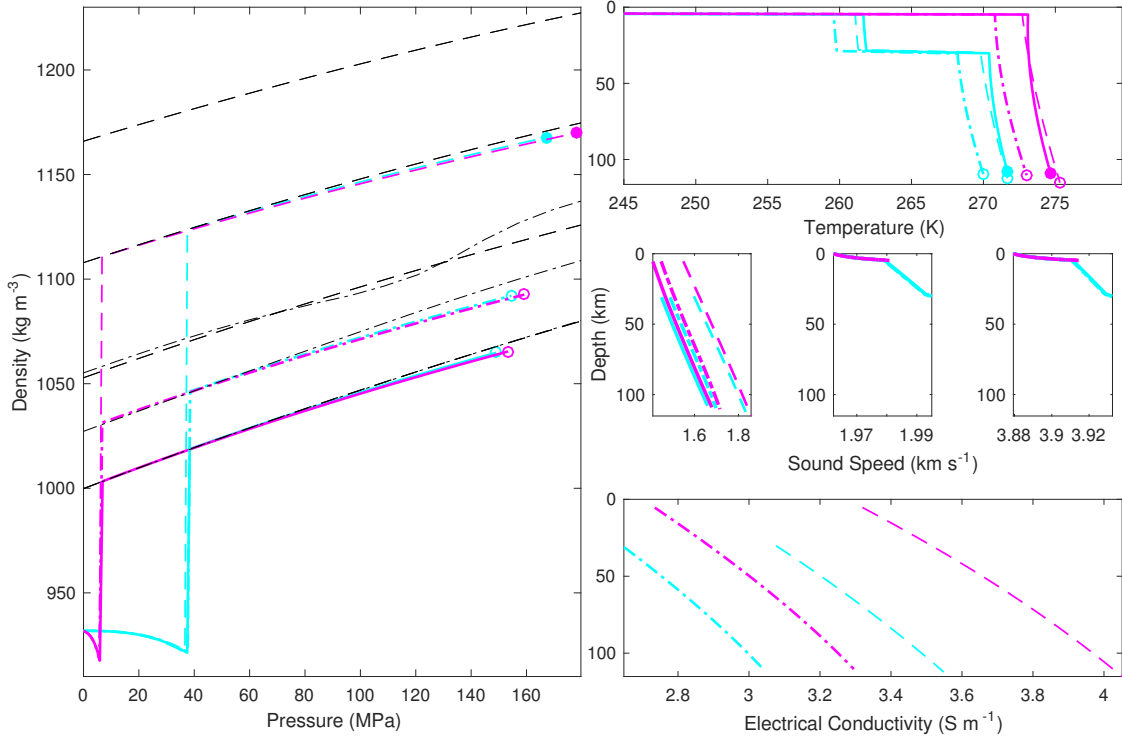


Figure 6. Europa: Oceans with 10 wt% MgSO₄(aq) (—), pure water (- -), and standard seawater ($S_0=35.165$ g per kg fluid; - · -) for T_b as in Table 6. Left: Density versus pressure. Reference fluid densities along the melting curve for MgSO₄ are {0,5,10,15} wt% and for seawater are {0,1,2} $\times S_0$. Right: Corresponding depth-dependent temperature (top), sound speed in the fluids and ices (fluid, V_S , V_P middle left to right), and electrical conductivity (bottom). Circles indicate the transition to the silicate interior.

in the south polar region, the depth of the silicate interior varies by up to 10 km with salinity due to the large proportional change in density of the volatile layer.

The small size of Enceladus precludes the existence of a metallic core. All models matching the bulk ice thickness of 50 km require a low rock density ($\approx 2700 \text{ kg m}^{-3}$). This is met by either a fully hydrous pyrolite (Table 7) or anhydrous and porous chondrite. The heat flux in the rocky interior is set to 0.27 GW. As shown in Fig. 10, porosity introduces a strong temperature dependence to density and sound speeds, reducing the density by up to more than 150% and sound velocity by up to more than 75%. If the 10 km ice thickness were the global value, the smaller rock density ($\approx 2200 \text{ kg m}^{-3}$) could be met by adding a combination of Na₂O, hydration, and porosity. The anelasticity of the rocky layer is high ($Q_S/\omega^\gamma > 10^7$) in all cases.

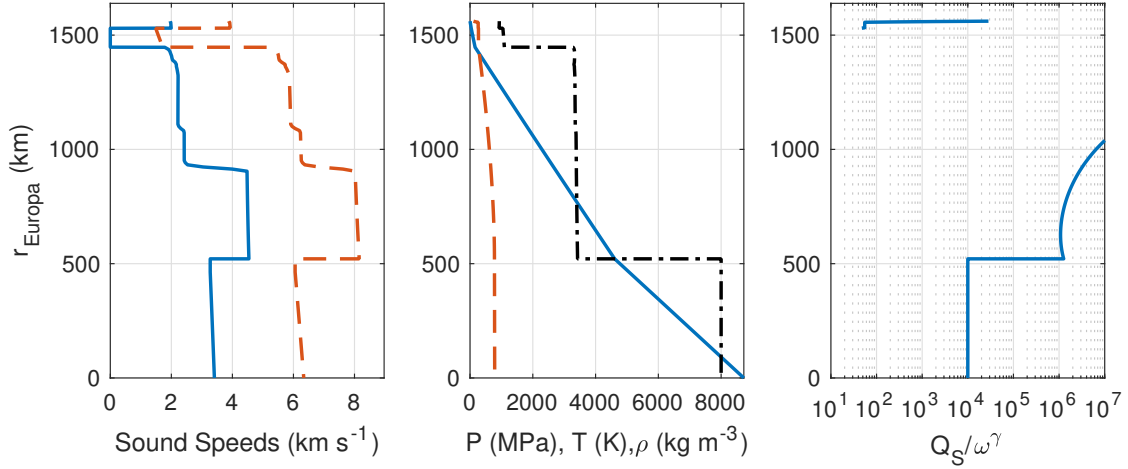


Figure 7. Europa: global interior structure for an ocean with the composition seawater and 30km-thick ice Ih lithosphere. Left: V_S (—) and V_P (---). Middle: Pressure (—), temperature (---), and density (· -). Right: Anelasticity.

3.4 Titan

Titan’s ice covering is interpreted to be 55-80 km based on the observed Schumann resonance [Béghin *et al.*, 2012]. We consider thicknesses in this range and approaching as much as 150 km.

We compare the effects of including small amounts of ammonia (3 wt%) or requiring a high salinity of MgSO_4 (10 wt%). The prevalence of reduced volatiles in Titan’s atmosphere and seas suggests against the more oxidized sulfate-rich ocean studied by Fortes *et al.* [2007]; Grindrod *et al.* [2008], but we consider sulfate due to the availability of the equation of state.

We consider models without a metallic core Figure 11 and Table 8. Heat flux in the rocky interior is set to 120 GW. For the pure water ocean (solid lines), ice V and VI are present, except in the warmest cases. For the highest bottom melting temperature ($T_b=270$ K), the ocean has no high pressure ices at all. Adding 3 wt% NH_3 to Titan’s ocean lowers the density and narrows the adiabat. The lower fluid compressibility corresponds to a higher sound speed. For the highest heat flow model (thinnest ice Ih), the ammonia and water oceans have little or no high pressure ice. The higher densities of the MgSO_4 oceans means high-pressure ices are thicker.

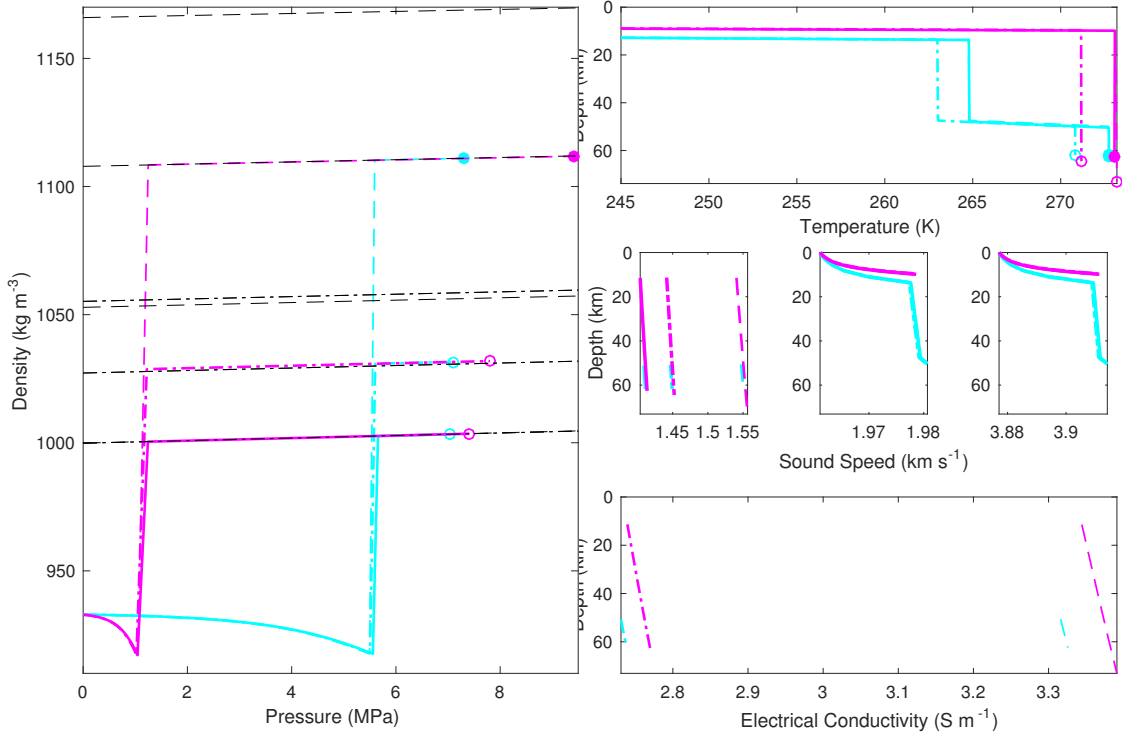


Figure 8. Enceladus: Oceans with 10 wt% MgSO₄(aq) (—), pure water (---), and standard seawater (— · —) for T_b as in Table 7. Left: Density versus pressure. Reference densities as for Europa (Fig. 6). Right: Corresponding depth-dependent temperature (top), sound speed in the fluids and ices (fluid, V_S , V_P middle left to right), and electrical conductivity (bottom). Circles indicate the transition to the silicate interior.

The required rock densities are low ($\approx 2600 \text{ kg m}^{-3}$), most consistent with the saturated chondrite composition.

3.5 Callisto

We consider ice thicknesses exceeding 100 km. For simplicity we do not modify the parameterization of solid state convection to accommodate a fully stagnant lid [McKinnon, 2006]. We consider oceans with 0 and 10 wt% MgSO₄.

Figure 13 shows interiors for both the reported value of Callisto’s gravitational moment of inertia [$C/MR^2 = 0.3549 \pm 0.0042$; Schubert *et al.*, 2004, Fig. 13] and a value that is 10% smaller [$C/MR^2 = 0.32$; Gao and Stevenson, 2013]. The higher value of C/MR^2 precludes the presence of a metallic core and requires a low silicate density around 3100 kg m^{-3} (Table 9), most consistent with the saturated pyrolite composition. Rock-interface depths of less

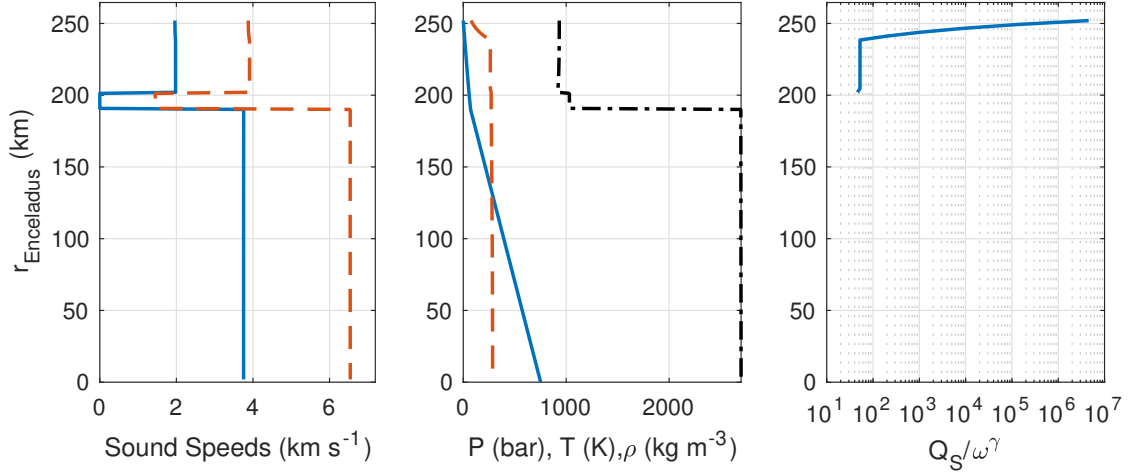


Figure 9. Enceladus: global interior structure with the ocean composition of seawater. Left: V_S (—) and V_P (---). Middle: Pressure (—), temperature (---), and density (·-). Right: Anelasticity.

than ~ 250 km are required. Ice VI does not occur. Buoyant ice III is present for the coldest oceans containing both pure water and salt. The smaller value of C/MR^2 leads to silicate depths similar to Ganymede’s (Table 10 and the likelihood of an iron core, specified as pure (γ) iron. Rock densities are best fit by the anhydrous pyrolite composition. Ice VI is always present, and buoyant ice III is present in the coldest model that includes salts.

4 Discussion

The computed profiles demonstrate the possible use of geophysical measurements to assess the habitability of ocean worlds. The combination of ocean salinity, bulk density, density structure, and ice I thickness constitute a combined constraint on the properties of the constituent materials, which must be logically consistent. Heat fluxes—which have yet to be measured directly—couple with salinity to determine which crystalline forms of ice are present in what amounts, and whether they will sink or float.

Consideration of the rocky layers of known ocean worlds suggests that a combination of measurements may reduce to a manageably short list or uniquely determine the possible combined properties of hydration state, porosity, and oxide content. For example, the oxide composition and hydration state create density signatures and phase boundaries that may be inferred from gravitational and seismic investigations, respectively.

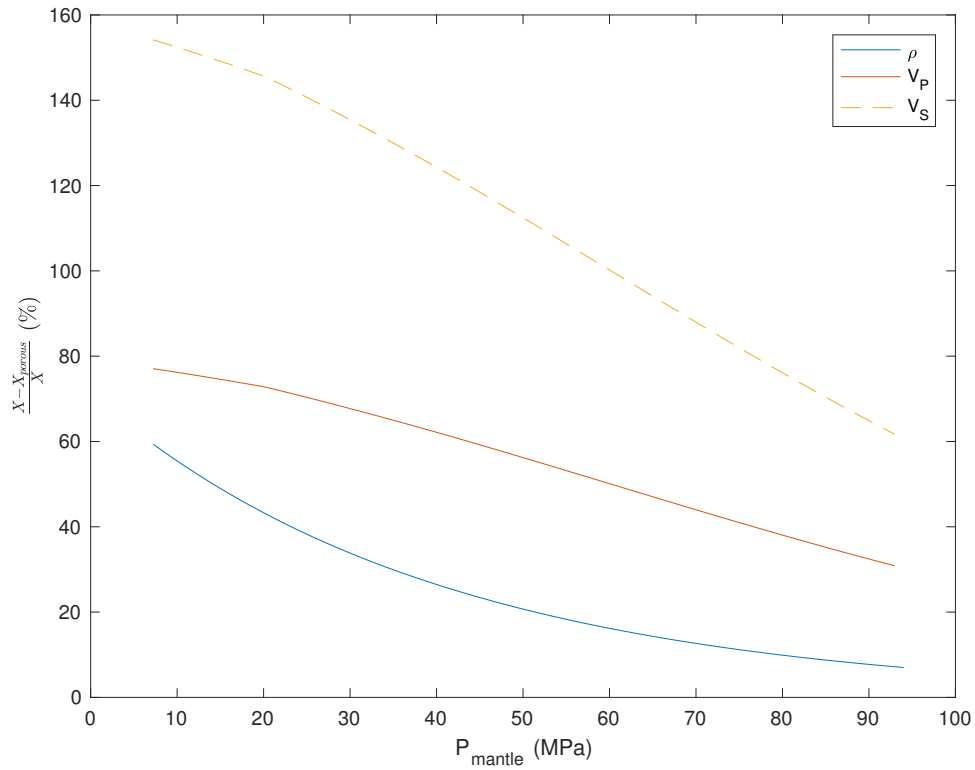


Figure 10. Enceladus: The influence of porosity on density, V_S (—) and V_P (---) for an anhydrous chondrite composition.

Water's main influence on density and seismic properties is to significantly reduce the solidus temperature. For scenarios that include a hot rocky interior, this may affect the viscoelastic relaxation of rocks, also at seismic frequencies (as later discussed in the anelasticity section) and already at temperatures lower than the solidus.

4.1 Tests for Habitability

Depth-dependent density, temperature, electrical conductivity, and sound speed can be used to locate liquid reservoirs and thus confirm water-rock interactions. Inferring ocean composition and pH implies a constraint on the integrated redox fluxes through time.

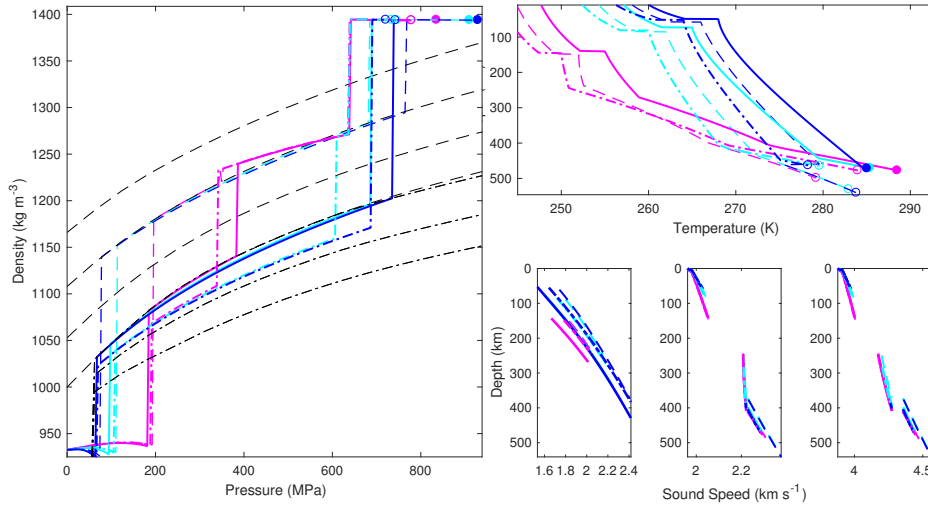


Figure 11. Titan: Oceans with 3 wt% $\text{NH}_3(\text{aq})$ (\cdots), pure water ($-$), and MgSO_4 ($--$) for T_b as in Table 8. Left: Density versus pressure. Reference fluid densities at {0,5,10} wt% for NH_3 decrease with increasing concentration, and increase for MgSO_4 . Right: Corresponding depth-dependent temperature (top), sound speeds in the fluids and ices (fluid, V_S , V_P bottom left to right). Circles denote the transition to the silicate interior.

4.1.1 Europa

The seawater and MgSO_4 oceans examined for Europa span the difference between oxidized and low-pH or reduced and high-pH, as simulated by *Zolotov* [2008]. For similar ice thicknesses, the higher-pH chloride ocean has a lower melting temperature, which dictates lower electrical conductivity, density, and sound speed. The first two of these will be constrained by gravity and electromagnetic experiments on the JUICE [*Grasset et al.*, 2013] and Europa [*Pappalardo et al.*, 2016] missions in combination with radar sounding and topographic imaging. A subsequent seismic experiment could address any degeneracies in interpreted ocean density and electrical conductivity by measuring the oceanic sound speed. Thermal radar mapping will establish the existence and characteristics of solid state convection, providing additional prior constraints for a follow-on seismic investigation. With this background established, it may be possible to determine the extent of aqueous alteration and sedimentation at the seafloor [*Vance et al.*, 2016b].

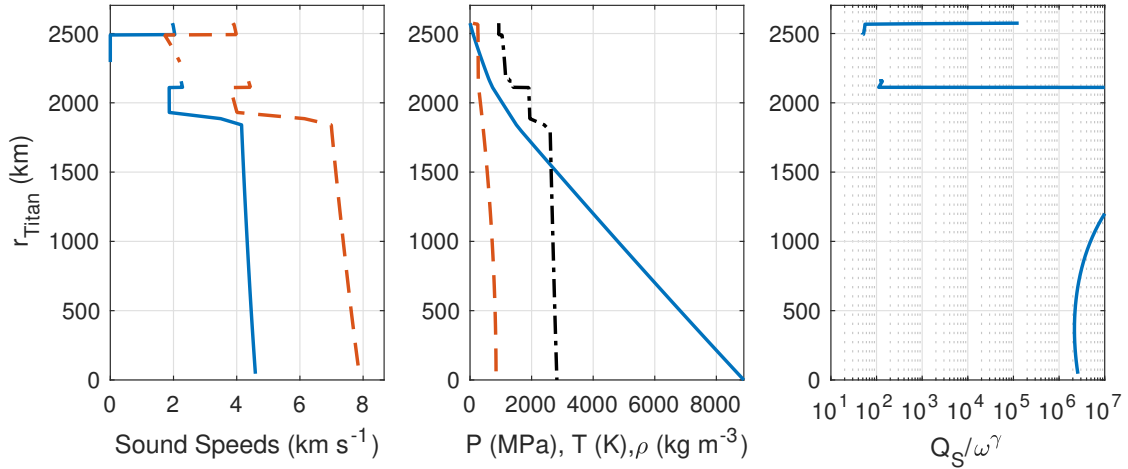


Figure 12. Titan: global interior structure for an ocean with 3 wt% $\text{NH}_3(\text{aq})$. Left: V_S (—) and V_P (---). Middle: Pressure (—), temperature (---), and density (- · -). Right: Anelasticity.

4.1.2 Enceladus

The silicate interior of Enceladus controls the extent of water rock interaction, including the production of hydrogen identified in south polar plume materials [Waite *et al.*, 2017]. Though it has previously suggested that the rocky core of Enceladus must be fully hydrated [Vance *et al.*, 2007, 2016a] as per the hydrous pyrolite model used here, the low pressures at Enceladus also permit an anhydrous chondrite composition with high porosities consistent with those in Earth's upper mantle. A transition from anhydrous to hydrous would explain the apparent present-day production of hydrogen [Hsu *et al.*, 2015], and might be consistent with recent activation or even formation of Enceladus [Čuk *et al.*, 2016].

Electromagnetic and seismic measurements could evaluate the extent and role of fluids and gases in south polar plume eruptions [Postberg *et al.*, 2011; Hsu *et al.*, 2015; Kite and Rubin, 2016]. By analogy with terrestrial investigations of geysers and volcanoes, a seismic experiment could reveal the flow rates, compositions, and geometry of plumes on Enceladus (Vance *et al.*, under revision; StÄdhler *et al.*, submitted). The seismic detectability of the strong influence of rock porosity on sound speed and density should be investigated.

4.1.3 Titan

A bulk ocean density of $> 1200 \text{ kg m}^{-3}$ is required of the large value of the measured tidal Love number ($k_2 > 0.6$) is correct Mitri *et al.* [2014]. The 10 wt% MgSO_4 ocean meets

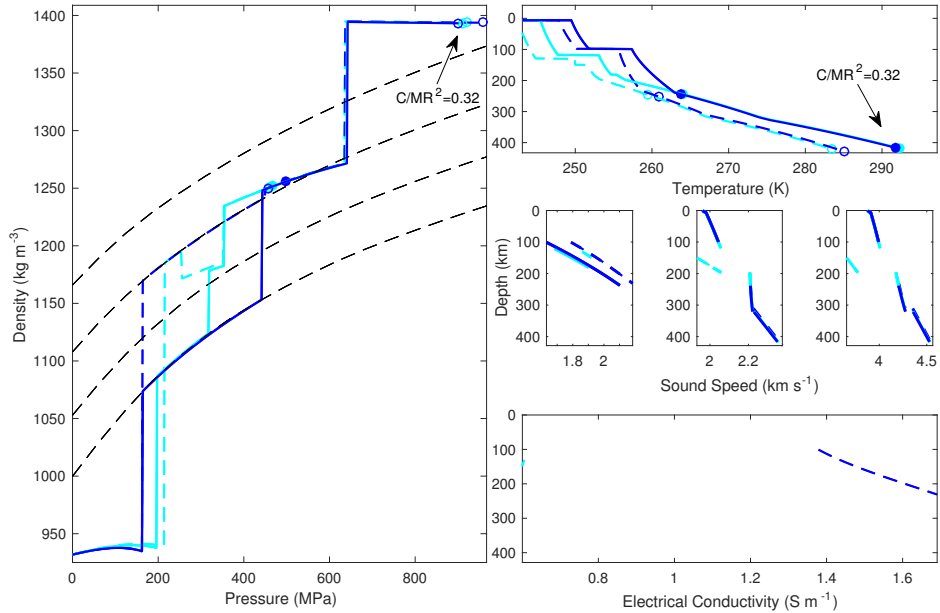


Figure 13. Callisto: Oceans with 10 wt% MgSO₄(aq) (—), pure water (---), and standard seawater (---) for T_b as in Table 9. Left: Density versus pressure. Reference densities as for Europa (Fig. 6). Right: Corresponding depth-dependent temperature (top), sound speed in the fluids and ices (fluid, V_S , V_P middle left to right), and electrical conductivity (bottom). Circles indicate the transition to the silicate interior. Greater silicate depths and pressures are also shown for the assumption of $C/MR^2=0.32$

this requirement. As noted above, a reducing ocean dominated instead by chlorides can obtain similarly large densities. A saline ocean is not required, however, as the uncertainty in the Love number ($k_2 = 0.637 \pm 0.220$) permits densities as low as 1100 kg m^{-3} , consistent with the pure water or 3 wt% cases studied here. A small core ($R < 400 \text{ km}$) coupled to a cold hydrous mantle, permitted by the gravitational constraints, would suggest an early hot Titan that lost most of its internal heat. A low heat flux in the deep interior is hard to reconcile with the inference that the ice is thinner than 100 km, unless the ice or ocean are tidally heated. If Titan’s ice is indeed thin and if the ocean has a low salinity, high-pressure ices may be minimal or absent entirely.

4.1.4 Ganymede

High-pressure ice phases V and VI, and possibly III, are likely present in Ganymede. The planned JUICE mission [Grasset *et al.*, 2013] will constrain the global density structure

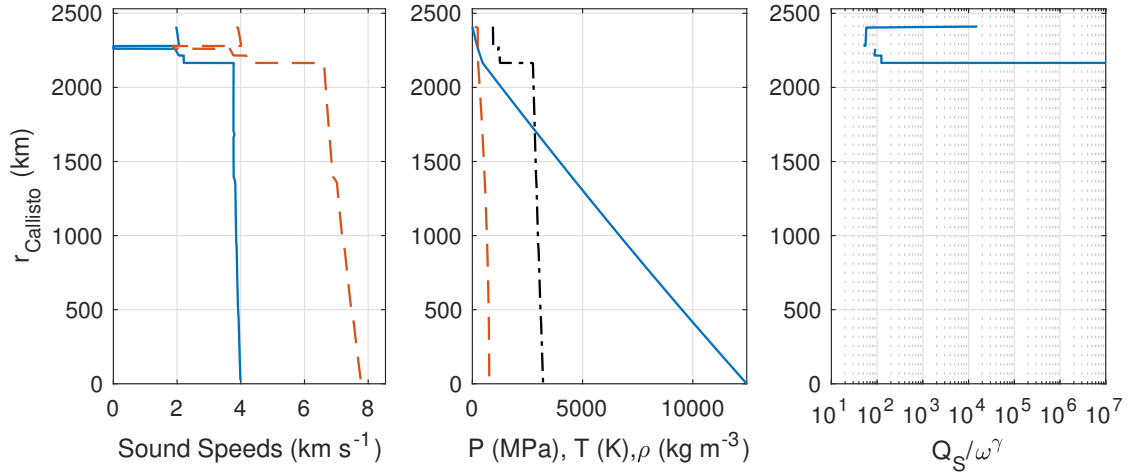


Figure 14. Callisto: global interior structure for an ocean with 10 wt% $\text{MgSO}_4(\text{aq})$. Left: V_S (—) and V_P (---). Middle: Pressure (—), temperature (---), and density (- · -). Right: Anelasticity.

of Ganymede, its ice Ih thickness, and the conductance of its ocean. Using this prior information, a seismic investigation could reveal the radial structures of the ices and search for any liquids within and between those layers, including the abundance of liquids at the water-rock interface.

4.1.5 Callisto

Poor constraints on Callisto’s density structure mean that its ocean can be either Europa-like, less than 250 km deep and containing scarce or no high-pressure ices, or Titan-like, with seafloor pressures approaching 800 MPa and the presence of ices V and VI. In either case, the fully stagnant surface suggests the ocean is nearly frozen and so is near-eutectic in composition. This should lead to a high electrical conductivity. Buoyant ice III may be present, unless the ocean contains strong freezing suppressants such as ammonia or methanol.

4.2 Thermodynamic properties

Examining the influence of composition on the geophysics and habitability of ocean worlds reveals which thermodynamic measurements are most needed.

Fluids: Evaluating the differences between high and low pH oceans in larger satellites [chloride vs sulfate; *Zolotov and Kargel, 2009*] requires high-pressure thermodynamic data for aqueous NaCl and mixtures with sulfates, including the associated melting point suppres-

sion of ices. Some of this information is available at pressures relevant to watery exoplanets [Journaux *et al.*, 2013; Mantegazzi *et al.*, 2013], but crucial measurements in the 0.1-1 GPa range of pressures are lacking.

The scope of the present electrical conductivity analyses is limited. A more rigorous treatment of conductivity should evaluate the limitations of available theory [Marshall, 1987]. Laboratory electrical conductivity measurements could test the extrapolations to high salinity assumed herein.

Solids: To accurately interpret seismic measurements in terrestrial glaciers and in ocean worlds, sound speed measurements are needed in ices Ih, II, III, V, and VI at temperatures other than -35°C . This will also enable the development of thermodynamic properties comparable to those available for fluids, and more comprehensive predictions of the melting curves of ices in the presence of salts. Related work, already in progress, is revealing possible importance of trapped ions within ices [Fortes and Choukroun, 2010; Journaux *et al.*, 2013, 2017]. The associated geophysical properties of these materials would enable investigations (seismic, gravitational, etc...) that might be pursued by future exploration missions.

5 Conclusions

Calculations of the radial compositional structure of icy ocean worlds demonstrate the utility of geophysical measurements as test for habitability. We have focused on the relation between ice thickness and ocean composition, building on more limited prior work [Vance *et al.*, 2014] to illustrate the unique 1D structures arising from the combination of melting-point suppression and density in single-component oceans containing aqueous MgSO_4 , NaCl (as seawater), and NH_3 . We have established the ability of the PlanetProfile model to accommodate additional ocean compositions as suitable thermodynamic data become available. Although we have limited the present suite of models to those with thermally conducting rocky interiors too cold to allow melts to form, we have established the ability to evaluate the influence of the rocky interior by considering different mineral and elemental compositions, hydration states, porosity, and heat content.

Future work focusing on specific worlds can make use of new thermodynamic data for fluids and solids to evaluate the couplings between rock and ocean composition, and the presence of various ice phases. Similarly, the properties of the iron core can be varied in con-

cert the rock composition to explore the parameter space of heat and metal content in the cores of Europa, Ganymede, and possibly Titan.

Model outputs are suitable as inputs to forward calculations of seismic propagation, gravitational moment of inertia, tidal Love numbers, and induced magnetic fields, and so can be used in the design, planning, and data analysis for geophysical investigations.

A: Model Details

A.1 Mass and Gravitational Moment of Inertia

The bulk mass of the planet M is the sum of nested spherical shells of radius r (thickness dr) with constant density $\rho(r)$:

$$\begin{aligned} M &= \int_M dm = 4\pi \int_{R_{sil}}^R \rho(r)r^2 dr + \frac{4\pi}{3}\rho_{sil}R_{sil}^3 \\ &= M_{H_2O} + \frac{4\pi}{3}\rho_{sil}R_{sil}^3 \end{aligned} \quad (\text{A.1})$$

where the M_{H_2O} includes the mass of the low-pressure ice upper layer, the ocean, and the high-pressure ice layers. The moment of inertia is:

$$\begin{aligned} C &= \int_M x^2 dm = \iiint r^4 \rho(r, \theta, \psi) \sin^3(\theta) dr d\theta d\psi \\ &= \frac{8\pi}{3} \int_{R_{sil}}^R \rho(r)r^4 dr + \frac{8\pi}{15}\rho_{sil}R_{sil}^5 \\ &= C_{H_2O} + \frac{8\pi}{15}\rho_{sil}R_{sil}^5 \end{aligned} \quad (\text{A.2})$$

where x is the distance of the element of mass (dm) from the spin axis. Starting from the surface ($R_{sil} = R - dr$), the radius of the silicate interface is decreased by dr . The overlying mass (M_{H_2O}) and moment of inertia (C_{H_2O}) are recomputed with each step. The solution of the interface radius (R_{sil}) provides the silicate density (ρ_{sil}) from Eq. A.1. The model uses this value to calculate the moment of inertia from Eq. A.2 for specified values of the temperature (T_b) at the base of the ice I layer and specified values of fluid salinity.

A.2 Silicate Interior

To predict the radii of the silicate/H₂O interface (R_{sil}) and iron core (R_{iron}), the model prescribes the densities of the silicates (ρ_{sil}) and the iron core (ρ_{core}). The moment of iner-

tia is then computed from:

$$M_{iron} = M - M_{H_2O} - \frac{4\pi}{3}\rho_{sil}(R_{sil}^3 - R_{iron}^3) \quad (A.3)$$

$$R_{iron} = \left(\frac{M - M_{H_2O} - \frac{4\pi}{3}\rho_{sil}R_{sil}^3}{\frac{4\pi}{3}(\rho_{iron} - \rho_{sil})} \right)^{1/3} \quad (A.4)$$

$$C = C_{H_2O} + \frac{8\pi}{15}(\rho_{sil}(R_{sil}^5 - R_{iron}^5) + \rho_{iron}R_{iron}^5) \quad (A.5)$$

If no iron core is present (as stipulated by the model), R_{sil} is a function of ρ_{sil} and C . In all cases, the model finds the range of values allowed by the bounded moment of inertia and chooses those corresponding to the nominal value of C .

Thermal Conduction in Ices

Thermally conductive profiles assume temperature-dependent conductivity of the form $k = D/T$, with temperature represented as a function of depth z as

$$T(z) = T_b \frac{z}{z_b} T_o \left(1 - \frac{z}{z_b}\right), \quad (A.6)$$

and corresponding heat flux at the ice I-water interface (z_b and T_b),

$$q_b = D \frac{\ln T_b/T_s}{z_b}. \quad (A.7)$$

Assuming $D = 632 \text{ W m}^{-1}$ for ice I provides accuracy of better than 10% in the range of temperatures from 100-270 K. Scalings other than T^{-1} from *Andersson and Inaba* [2005] are refit to match the middle of the provided range of temperature with a loss of accuracy of less than 5%. In the calculation of solid state convection, k is computed from the fits recommended by *Andersson and Inaba* [2005].

Thermal Conduction in Rock

The temperature profile in the rocky interior is computed by the same method as in *Cammarano et al.* [2006]:

$$T(r) = T_0 + \frac{\rho_{rock}H}{6k}(a^2 - r^2) + \left(\frac{\rho_{rock}Hr_b^3}{3k} - \frac{q_b r_b^2}{k} \right) \left(\frac{1}{a} - \frac{1}{r} \right) \quad (A.8)$$

Inputs to PlanetProfile are: ρ_{rock} , the mean silicate density specified as an input; H , the rate of heat production per unit mass ($H = Q/M$, determined from input of Q in W m^{-2}); and k , the thermal conductivity of the rock. The remaining variables are determined by the model: T_0 , the temperature at the top of the silicate layer; and a and r_b , the radius at the top and bottom of the silicate layer, respectively. The heat flow at the base of the rock layer, q_b , is set

to zero. Thermal conductivity is the same as that specified by *Cammarano et al.* [2006]:

$$k = 4.0 \text{ W (m K)}^1.$$

A.3 Solid State Convection in Ices

Solid state convection in ice Ih is from the parameterization *Deschamps and Sotin* [2001] based on numerical experiments and known material properties. The critical Rayleigh number

$$Ra = \frac{\alpha \rho g \Delta T h^3}{\kappa \mu} \quad (\text{A.9})$$

is determined at the characteristic temperature of the well-mixed convective interior of the ice:

$$T_c = B \left[\sqrt{1 + \frac{2}{B}(T_m - C)} - 1 \right], B = \frac{E}{2Rc_1}, C = c_2 \Delta T \quad (\text{A.10})$$

in which T_m is the characteristic melting temperature, specified as temperature at the ice-liquid interface, E is the activation energy of the material (Table A.1), R is the ideal gas constant (8.314 J mole⁻¹ K⁻¹), $c_1 = 1.43$, $c_2 = -0.03$, and $\Delta T = T_m - T_{top}$. The Newtonian viscosity is

$$\mu = \mu_0 \exp \left[A \left(\frac{T_m}{T} - 1 \right) \right], A = \frac{E}{RT_m} \quad (\text{A.11})$$

with coefficient μ_0 specified in Table A.1.

The lower thermal boundary layer scales with Rayleigh number as $Ra_\delta = 0.28 Ra^{0.21}$.

The boundary layer's thickness is

$$\delta = \left[\frac{\mu_c \kappa}{\alpha \rho g (T_m - T_c)} Ra_\delta \right]^{1/3} \quad (\text{A.12})$$

and the corresponding heat flux is

$$Q = \frac{k(T_m - T_c)}{\delta}. \quad (\text{A.13})$$

The temperature of the overlying brittle lithosphere is scaled as $T_{lith} = T_{top} + 0.3 \Delta T$

The thermal boundary layer thickness is

$$e_{TBL} = \frac{k_{ice}(T_{lith} - T_{top})}{Q}. \quad (\text{A.14})$$

Acknowledgments

The PlanetProfile model and applications described in this work are available online (<https://github.com/vancesteven/PlanetProfile>) and support for its use may be obtained from the author via email. Work by JPL co-authors was partially supported by strategic research and technology funds from the Jet Propulsion

Laboratory, Caltech, and by the Icy Worlds node of NASA's Astrobiology Institute (13-13NAI7_2-0024). SDV acknowledges the support of NASA Outer Planets Research Grant NNN12ZDA001N "Solution Thermochemistry Relevant to Outer Planets and Satellites". RL acknowledges the support of NASA Outer Planets Research Grant NNX13AK97G "Physical Processes in Titan's Seas". SCS was supported by grant SI1538/4-1 of Deutsche Forschungsgemeinschaft *DFG*. No conflicts of interest are identified associated with this work. A part of the research was carried out at the Jet Propulsion Laboratory, California Institute of Technology, under a contract with the National Aeronautics and Space Administration. Copyright 2017. All rights reserved.

References

- Anderson, J., G. Schubert, R. Jacobson, E. Lau, W. Moore, and W. Sjogren (1998), Europa's differentiated internal structure: inferences from four Galileo encounters, *Science*, *281*(5385), 2019 – 2022.
- Andersson, O., and A. Inaba (2005), Thermal conductivity of crystalline and amorphous ices and its implications on amorphization and glassy water, *Phys. Chem. Chem. Phys.*, *7*(7), 1441–1449.
- Béghin, C., O. Randriamboarison, M. Hamelin, E. Karkoschka, C. Sotin, R. C. Whitten, J.-J. Berthelier, R. Grard, and F. Simões (2012), Analytic theory of Titan's Schumann resonance: Constraints on ionospheric conductivity and buried water ocean, *Icarus*, *218*(2), 1028–1042.
- Bell, R., D. Blankenship, C. Finn, D. Morse, T. Scambos, J. Brozina, and S. Hodge (1998), Influence of subglacial geology on the onset of a west antarctic ice stream from aerogeophysical observations, *Nature*, *394*(6688), 58–62.
- Beuthe, M. (2016), Crustal control of dissipative ocean tides in Enceladus and other icy moons, *Icarus*, *280*, 278–299.
- Bland, M., A. Showman, and G. Tobie (2009), The orbital–thermal evolution and global expansion of Ganymede, *Icarus*, *200*(1), 207–221.
- Bland, M. T., and W. B. McKinnon (2015), Forming ganymede's grooves at smaller strain: toward a self-consistent local and global strain history for ganymede, *Icarus*, *245*, 247–262.
- Brown, M., and K. Hand (2013), Salts and radiation products on the surface of Europa, *The Astronomical Journal*, *145*(4), 110.

- Cammarano, F., V. Lekic, M. Manga, M. Panning, and B. Romanowicz (2006), Long-period seismology on Europa: 1. physically consistent interior models, *Journal of Geophysical Research*, *E12009*, doi:10.1029/2006JE002,710.
- Cammarano, F., P. Tackley, and L. Boschi (2011), Seismic, petrological and geodynamical constraints on thermal and compositional structure of the upper mantle: global thermo-chemical models, *Geophysical Journal International*, *187*(3), 1301–1318.
- Carlson, R. (2014), The influence of porosity and crack morphology on seismic velocity and permeability in the upper oceanic crust, *Geochemistry, Geophysics, Geosystems*, *15*(1), 10–27.
- Catling, D. C., and M. W. Claire (2005), How Earth's atmosphere evolved to an oxic state: a status report, *Earth and Planetary Science Letters*, *237*(1), 1–20.
- Choblet, G., G. Tobie, C. Sotin, K. Kalousová, and O. Grasset (2017), Heat transport in the high-pressure ice mantle of large icy moons., *Icarus*, *285*, 252–262.
- Choukroun, M., and O. Grasset (2010), Thermodynamic data and modeling of the water and ammonia-water phase diagrams up to 2.2 GPa for planetary geophysics, *The Journal of Chemical Physics*, *133*, 144,502.
- Christensen, N. I. (1989), Pore pressure, seismic velocities, and crustal structure, *Geological Society of America Memoirs*, *172*, 783–798.
- Connolly, J. (2005), Computation of phase equilibria by linear programming: a tool for geodynamic modeling and its application to subduction zone decarbonation, *Earth and Planetary Science Letters*, *236*(1), 524–541.
- Connolly, J. (2009), The geodynamic equation of state: what and how, *Geochemistry, Geophysics, Geosystems*, *10*(10).
- Ćuk, M., L. Dones, and D. Nesvorný (2016), Dynamical evidence for a late formation of Saturn's moons, *The Astrophysical Journal*, *820*(2), 97.
- Darot, M., and T. Reuschlé (2000), Effect of pore and confining pressures on vp in thermally pre-cracked granites, *Geophysical research letters*, *27*(7), 1057–1060.
- Deschamps, F., and C. Sotin (2001), Thermal convection in the outer shell of large icy satellites, *Journal of Geophysical Research-Planets*, *106*(E3), 5107–5121.
- Diez, A. (2013), Effects of cold glacier ice crystal anisotropy on seismic data, Ph.D. thesis.
- Durham, W., S. Kirby, and L. Stern (2001), Rheology of water ice — Applications to satellites of the outer planets, *Annual Review of Earth and Planetary Sciences*, *29*, 295–330.

- Hand, K., and C. Chyba (2007), Empirical constraints on the salinity of the European ocean and implications for a thin ice shell, *Icarus*, *189*(2), 424–438.
- Hand, K., R. Carlson, and C. Chyba (2007), Energy, chemical disequilibrium, and geological constraints on Europa, *Astrobiology*, *7*(6), 1006–1022.
- Hayes, J. M., and J. R. Waldbauer (2006), The carbon cycle and associated redox processes through time, *Philosophical Transactions of the Royal Society B: Biological Sciences*, *361*(1470), 931–950.
- Helfrich, G., and J. Connolly (2009), Physical contradictions and remedies using simple polythermal equations of state, *American Mineralogist*, *94*(11-12), 1616–1619.
- Hogenboom, D. L., J. S. Kargel, J. P. Ganasan, and L. Lee (1995), Magnesium sulfate-water to 400 MPa using a novel piezometer: Densities, phase equilibria, and planetological implications, *Icarus*, *115*(2), 258–277.
- Holland, T., and R. Powell (2011), An improved and extended internally consistent thermodynamic dataset for phases of petrological interest, involving a new equation of state for solids, *Journal of Metamorphic Geology*, *29*(3), 333–383.
- Hsu, H.-W., F. Postberg, Y. Sekine, T. Shibuya, S. Kempf, M. Horányi, A. Juhász, N. Altobelli, K. Suzuki, Y. Masaki, et al. (2015), Ongoing hydrothermal activities within Enceladus, *Nature*, *519*(7542), 207–210.
- Iess, L., R. Jacobson, M. Ducci, D. Stevenson, J. Lunine, J. Armstrong, S. Asmar, P. Racioppa, N. Rappaport, and P. Tortora (2012), The tides of Titan, *Science*, *337*(6093), 457–459.
- Iess, L., D. J. Stevenson, M. Parisi, D. Hemingway, R. A. Jacobson, J. I. Lunine, F. Nimmo, J. W. Armstrong, S. W. Asmar, M. Ducci, and P. Tortora (2014), The gravity field and interior structure of Enceladus, *Science*, *344*(6179), 78–80.
- Jacobson, R., P. Antreasian, J. Bordi, K. Criddle, R. Ionascu, J. Jones, R. Mackenzie, M. Meek, D. Parcher, F. Pelletier, et al. (2006), The Gravity Field of the Saturnian System from Satellite Observations and Spacecraft Tracking Data, *The Astronomical Journal*, *132*(6), 2520–2526.
- Journaux, B., I. Daniel, R. Caracas, G. Montagnac, and H. Cardon (2013), Influence of NaCl on ice VI and ice VII melting curves up to 6 GPa, implications for large icy moons, *Icarus*, *226*, 355–363.
- Journaux, B., I. Daniel, S. Petitgirard, H. Cardon, J.-P. Perrillat, R. Caracas, and M. Mezouar (2017), Salt partitioning between water and high-pressure ices. implication for the dynam-

- ics and habitability of icy moons and water-rich planetary bodies, *Earth and Planetary Science Letters*, 463, 36 – 47, doi:<http://dx.doi.org/10.1016/j.epsl.2017.01.017>.
- Kern, H. (1990), Laboratory seismic measurements: an aid in the interpretation of seismic field data, *Terra Nova*, 2(6), 617–628.
- Kite, E. S., and A. M. Rubin (2016), Sustained eruptions on Enceladus explained by turbulent dissipation in tiger stripes, *Proceedings of the National Academy of Sciences*, 113(15), 3972–3975.
- Kivelson, M., K. Khurana, and M. Volwerk (2002), The permanent and inductive magnetic moments of Ganymede, *Icarus*, 157(2), 507–522.
- Kozlovsky, Y. A. (1987), Geothermic investigations, in *The Superdeep Well of the Kola Peninsula*, pp. 387–393, Springer.
- Larionov, E. G., and P. A. Kryukov (1984), The conductivity of MgSO₄ aqueous-solutions in the range of temperatures 298-423K and pressures 0,1-784,6 MPa, *Izvestiya Sibirskogo Otdeleniya Akademii Nauk SSSR Seriya Khimicheskikh Nauk*, (5), 20–23.
- Ligier, N., F. Poulet, J. Carter, R. Brunetto, and F. Gourgéot (2016), Vlt/sinfoni observations of europa: New insights into the surface composition, *The Astronomical Journal*, 151(6), 163.
- Lyons, T. W., C. T. Reinhard, and N. J. Planavsky (2014), The rise of oxygen in earth's early ocean and atmosphere, *Nature*, 506(7488), 307–315.
- Mantegazzi, D., C. Sanchez-Valle, and T. Driesner (2013), Thermodynamic properties of aqueous NaCl solutions to 1073 K and 4.5 GPa, and implications for dehydration reactions in subducting slabs, *Geochimica et Cosmochimica Acta*, 121, 263–290.
- Marshall, W. L. (1987), Reduced state relationship for limiting electrical conductances of aqueous ions over wide ranges of temperature and pressure, *The Journal of chemical physics*, 87(6), 3639–3643.
- Maus, S., S. Müller, J. Büttner, S. Brütsch, T. Huthwelker, M. Schwikowski, F. Enzmann, and A. Vähätölo (2011), Ion fractionation in young sea ice from Kongsfjorden, Svalbard, *Annals of Glaciology*, 52(57), 301–310.
- McDougall, T. J., and P. M. Barker (2011), Getting started with TEOS-10 and the Gibbs Seawater (GSW) oceanographic toolbox, *SCOR/IAPSO WG*, 127, 1–28.
- McKinnon, W. (2006), On convection in ice shells of outer solar system bodies, with detailed application to Callisto, *Icarus*, 183(2), 435–450.

- McKinnon, W. B. (2015), Effect of Enceladus's rapid synchronous spin on interpretation of Cassini gravity, *Geophysical Research Letters*, *42*(7), 2137–2143.
- Mitri, G., R. Meriggiola, A. Hayes, A. Lefevre, G. Tobie, A. Genova, J. I. Lunine, and H. Zebker (2014), Shape, topography, gravity anomalies and tidal deformation of Titan, *Icarus*, *236*, 169–177.
- Müntener, O. (2010), Serpentine and serpentinization: a link between planet formation and life, *Geology*, *38*(10), 959–960.
- O'Brien, D. P., P. Geissler, and R. Greenberg (2002), A melt-through model for chaos formation on Europa, *Icarus*, *156*(152-161).
- Pappalardo, R., L. Prockter, D. Senske, R. Klima, S. Fenton Vance, and K. Craft (2016), Science objectives and capabilities of the NASA Europa Mission, in *Lunar and Planetary Science Conference*, vol. 47, p. 3058.
- Pasek, M. A., and R. Greenberg (2012), Acidification of Europa's subsurface ocean as a consequence of oxidant delivery, *Astrobiology*, *12*(2), 151–159.
- Peacock, S. M., N. I. Christensen, M. G. Bostock, and P. Audet (2011), High pore pressures and porosity at 35 km depth in the cascadia subduction zone, *Geology*, *39*(5), 471–474.
- PERPLEX (), 2016. <http://www.perplex.ethz.ch/>.
- Postberg, F., J. Schmidt, J. Hillier, S. Kempf, and R. Srama (2011), A salt-water reservoir as the source of a compositionally stratified plume on Enceladus, *Nature*, *474*(7353), 620–622.
- Saito, S., M. Ishikawa, M. Arima, and Y. Tatsumi (2016), Laboratory measurements of v_p and v_s in a porosity-developed crustal rock: Experimental investigation into the effects of porosity at deep crustal pressures, *Tectonophysics*, *677*, 218–226.
- Sanloup, C., F. Guyot, P. Gillet, G. Fiquet, M. Mezouar, and I. Martinez (2000), Density measurements of liquid Fe-S alloys at high-pressure, *Geophys. Res. Lett.*, *27*(6), 811–814.
- Schmidt, C., and C. Manning (2017), Pressure-induced ion pairing in mgso_4 solutions: Implications for the oceans of icy worlds, *Geochemical Perspectives Letters*, *3*, 66–74.
- Schubert, G., J. Anderson, T. Spohn, and W. McKinnon (2004), Interior composition, structure and dynamics of the Galilean satellites, *Jupiter: The Planet, Satellites and Magnetosphere*, pp. 281–306.
- Shaw, G. H. (1986), Elastic properties and equation of state of high pressure ice, *The Journal of Chemical Physics*, *84*(10), 5862–5868.

- Sotin, C., G. Tobie, J. Wahr, and W. McKinnon (2009), *Europa*, chap. Tides and tidal heating on Europa, pp. 85–117, University of Arizona Press, Tucson.
- Stixrude, L., and C. Lithgow-Bertelloni (2011), Thermodynamics of mantle minerals-II. phase equilibria, *Geophysical Journal International*, *184*(3), 1180–1213.
- Thomas, P. (2010), Sizes, shapes, and derived properties of the saturnian satellites after the cassini nominal mission, *Icarus*, *208*(1), 395–401.
- Thomas, P., R. Tajeddine, M. Tiscareno, J. Burns, J. Joseph, T. Lored, P. Helfenstein, and C. Porco (2016), Enceladus’s measured physical libration requires a global subsurface ocean, *Icarus*, *264*, 37–47.
- Tillner-Roth, R., and D. G. Friend (1998), A Helmholtz free energy formulation of the thermodynamic properties of the mixture {water+ ammonia}, *Journal of Physical and Chemical Reference Data*, *27*(1), 63–96.
- Todd, T., and G. Simmons (1972), Effect of pore pressure on the velocity of compressional waves in low-porosity rocks, *Journal of Geophysical Research*, *77*(20), 3731–3743.
- Tutolo, B. M., D. F. Mildner, C. V. Gagnon, M. O. Saar, and W. E. Seyfried (2016), Nanoscale constraints on porosity generation and fluid flow during serpentinization, *Geology*, *44*(2), 103–106.
- Ulmer, P., and V. Trommsdorff (1995), Serpentine stability to mantle depths and subduction-related magmatism, *Science*, *268*(5212), 858.
- Vance, S., and J. Brown (2013), Thermodynamic properties of aqueous MgSO₄ to 800 MPa at temperatures from -20 to 100 °C and concentrations to 2.5 mol kg⁻¹ from sound speeds, with applications to icy world oceans, *Geochimica et Cosmochimica Acta*, *110*, 176–189.
- Vance, S., J. Harnmeijer, J. Kimura, H. Hussmann, B. deMartin, and J. M. Brown (2007), Hydrothermal systems in small ocean planets, *Astrobiology*, *7*(6), 987–1005.
- Vance, S., M. Bouffard, M. Choukroun, and C. Sotin (2014), Ganymede’s internal structure including thermodynamics of magnesium sulfate oceans in contact with ice, *Planetary And Space Science*, *96*, 62–70.
- Vance, S., J. M. Brown, O. Bollengier, B. G. Bills, J. C. Castillo, M. Choukroun, J. M. Jackson, S. Kedar, and V. C. Tsai (2015), Thermodynamics and interior structure measurements of ocean worlds, in *2015 AGU Fall Meeting*, Agu.
- Vance, S., K. Hand, and R. Pappalardo (2016a), Geophysical controls of chemical disequilibria in Europa, *Geophysical Research Letters*, *10.1002/2016GL068547*.

- Vance, S., V. Tsai, S. Kedar, B. Bills, J. Castillo-Rogez, and J. Jackson (2016b), Seismic investigations of Europa and other ocean worlds, in *EGU General Assembly Conference Abstracts*, vol. 18, p. 5372.
- Vitovtova, V., V. Shmonov, and A. Zharikov (2014), The porosity trend and pore sizes of the rocks in the continental crust of the earth: Evidence from experimental data on permeability, *Izvestiya, Physics of the Solid Earth*, 50(5), 593–602.
- Vogt, C., K. Laihem, and C. Wiebusch (2008), Speed of sound in bubble-free ice, *The Journal of the Acoustical Society of America*, 124(6), 3613–3618.
- Waite, J. H., C. R. Glein, R. S. Perryman, B. D. Teolis, B. A. Magee, G. Miller, J. Grimes, M. E. Perry, K. E. Miller, A. Bouquet, et al. (2017), Cassini finds molecular hydrogen in the Enceladus plume: Evidence for hydrothermal processes, *Science*, 356(6334), 155–159.
- Wang, X.-Q., A. Schubnel, J. Fortin, E. David, Y. Guéguen, and H.-K. Ge (2012), High v_p/v_s ratio: Saturated cracks or anisotropy effects?, *Geophysical Research Letters*, 39(11).
- Wyllie, M., A. Gregory, and G. Gardner (1958), An experimental investigation of factors affecting elastic wave velocities in porous media, *Geophysics*, 23(3), 459–493.
- Yu, C., S. Ji, and Q. Li (2016), Effects of porosity on seismic velocities, elastic moduli and Poisson's ratios of solid materials and rocks, *Journal of Rock Mechanics and Geotechnical Engineering*, 8(1), 35–49.
- Zolotov, M. (2008), Oceanic composition on Europa: Constraints from mineral solubilities, in *Lunar and Planetary Institute Science Conference Abstracts*, vol. 39, p. 2349.
- Zolotov, M. Y., and J. Kargel (2009), On the chemical composition of Europa's icy shell, ocean, and underlying rocks, *Europa*, edited by RT Pappalardo, WB McKinnon, and K. Khurana, University of Arizona Press, Tucson, AZ, pp. 431–458.

MgSO ₄ 10wt%	ρ_{rock} (kg m ⁻³)	3450		
	$\rho_{rock,model}$ (kg m ⁻³)	3457	3456	3456
	T_b (K)	252	260	270
	q_b mW m ⁻²	4	6	22
	q_c mW m ⁻²	15	18	25
	D_{Ih} (km)	142	95	26
	D_{ocean} (km)	75	288	650
	D_{III} (km)	16	-	-
	D_V (km)	152	-	-
	D_{VI} (km)	479	501	231
	R_{rock} (km)	1770	1750	1727
	R_{core} (km)	589	629	680
Water	ρ_{rock} (kg m ⁻³)	3450		
	$\rho_{rock,model}$ (kg m ⁻³)	3456	3457	3458
	T_b (K)	255	265	273
	q_b mW m ⁻²	4	8	107
	q_c mW m ⁻²	16	20	107
	D_{Ih} (km)	134	70	5
	D_{ocean} (km)	117	375	603
	D_V (km)	144	-	-
	D_{VI} (km)	452	386	215
	R_{rock} (km)	1787	1803	1811
	R_{core} (km)	537	490	479

Table 5. Ganymede: chondrite composition with 1 wt% hydration. $Q_{rock} = 400$ GW.

MgSO ₄ 10wt%	ρ_{rock} (kg m ⁻³)	3300	
	$\rho_{rock,model}$ (kg m ⁻³)	3375	3375
	T_b (K)	269.80	272.70
	q_b mW m ⁻²	19	123
	q_c mW m ⁻²	24	123
	D_{Ih} (km)	30	5
	D_{ocean} (km)	88	116
	R_{rock} (km)	1443	1440
	R_{core} (km)	522	523
	Water	ρ_{rock} (kg m ⁻³)	3300
$\rho_{rock,model}$ (kg m ⁻³)		3375	3374
T_b (K)		270.40	273.10
q_b mW m ⁻²		19	119
q_c mW m ⁻²		24	119
D_{Ih} (km)		30	5
D_{ocean} (km)		83	109
R_{rock} (km)		1448	1447
R_{core} (km)		521	521
Seawater 35.165g/kg		ρ_{rock} (kg m ⁻³)	3300
	$\rho_{rock,model}$ (kg m ⁻³)	3375	3375
	X_{FeS} (%)	0	
	T_b (K)	268.20	270.80
	q_b mW m ⁻²	18	121
	q_c mW m ⁻²	23	121
	D_{Ih} (km)	30	5
	D_{ocean} (km)	84	111
	R_{rock} (km)	1447	1446
	R_{core} (km)	521	520

Table 6. Europa:pyrolite composition with Na₂O. $Q_{rock} = 100$ GW.

MgSO ₄ 10wt%	ρ_{rock} (kg m ⁻³)	2701	2265
	$\rho_{rock,model}$ (kg m ⁻³)	2698	2697
	T _b (K)	272.72	273.12
	q _b mW m ⁻²	16	83
	q _c mW m ⁻²	10	83
	D _{Ih} (km)	50	10
	D _{ocean} (km)	13	63
	R _{rock} (km)	190	179
Seawater 35.165g/kg	ρ_{rock} (kg m ⁻³)	2669	2222
	$\rho_{rock,model}$ (kg m ⁻³)	2698	2698
	T _b (K)	270.82	271.16
	q _b mW m ⁻²	16	84
	q _c mW m ⁻²	10	84
	D _{Ih} (km)	50	10
	D _{ocean} (km)	12	55
	R _{rock} (km)	190	188
Water	ρ_{rock} (kg m ⁻³)	2668	2216
	$\rho_{rock,model}$ (kg m ⁻³)	2698	2697
	T _b (K)	272.74	273.08
	q _b mW m ⁻²	16	83
	q _c mW m ⁻²	10	83
	D _{Ih} (km)	50	10
	D _{ocean} (km)	11	53
	R _{rock} (km)	190	189
NH ₃ 3wt%	ρ_{rock} (kg m ⁻³)	2651	2210
	$\rho_{rock,model}$ (kg m ⁻³)	2698	2698
	T _b (K)	269.54	269.90
	q _b mW m ⁻²	16	81
	q _c mW m ⁻²	10	81
	D _{Ih} (km)	50	10
	D _{ocean} (km)	12	51
	R _{rock} (km)	191	191

Table 7. Enceladus: saturated pyrolyte composition. $Q_{rock} = 0.27$ GW.

MgSO ₄ 10wt%	ρ_{rock} (kg m ⁻³)	2616	2545	2524
	$\rho_{rock,model}$ (kg m ⁻³)	2623	2562	2468
	Q_{rock} (GW)	120		
	T_b (K)	252	262	266
	q_b mW m ⁻²	4	8	11
	q_c mW m ⁻²	14	17	19
	D_{Ih} (km)	149	86	58
	D_{ocean} (km)	91	333	403
	D_V (km)	163	-	-
	D_{VI} (km)	96	111	79
	R_{rock} (km)	2076	2044	2034
	Water	ρ_{rock} (kg m ⁻³)	2540	2527
$\rho_{rock,model}$ (kg m ⁻³)		2611	2598	2591
Q_{rock} (GW)		120		
T_b (K)		255	265	268
q_b mW m ⁻²		4	9	13
q_c mW m ⁻²		14	18	20
D_{Ih} (km)		141	74	50
D_{ocean} (km)		130	369	420
D_V (km)		140	-	-
D_{VI} (km)		67	27	2
R_{rock} (km)		2097	2104	2103
NH ₃ 3wt%		ρ_{rock} (kg m ⁻³)	2531	2523
	$\rho_{rock,model}$ (kg m ⁻³)	2612	2603	2601
	Q_{rock} (GW)	120		
	T_b (K)	250	260	264
	q_b mW m ⁻²	4	8	12
	q_c mW m ⁻²	13	17	19
	D_{Ih} (km)	146	82	52
	D_{ocean} (km)	100	321	396
	D_V (km)	164	16	-
	D_{VI} (km)	68	46	15
	R_{rock} (km)	2097	2110	2112

Table 8. Titan: saturated chondrite composition. $Q_{rock} = 120$ GW.

MgSO ₄	ρ_{rock} (kg m ⁻³)	3118	3054
10wt%	$\rho_{rock,model}$ (kg m ⁻³)	2933	2935
	T_b (K)	250	255.70
	q_b mW m ⁻²	4	5
	q_c mW m ⁻²	16	18
	D_{Ih} (km)	130	100
	D_{ocean} (km)	20	132
	D_{III} (km)	46	-
	D_V (km)	120	79
	R_{rock} (km)	2165	2158
Water	ρ_{rock} (kg m ⁻³)	3094	3077
	$\rho_{rock,model}$ (kg m ⁻³)	2936	2937
	T_b (K)	253.10	257.40
	q_b mW m ⁻²	4	5
	q_c mW m ⁻²	17	18
	D_{Ih} (km)	120	100
	D_{ocean} (km)	62	139
	D_{III} (km)	16	-
	D_V (km)	121	83
	R_{rock} (km)	2166	2166

Table 9. Callisto: saturated pyrolite composition. $Q_{rock} = 110$ GW

MgSO ₄ 10wt%	ρ_{rock} (kg m ⁻³)	3500	
	$\rho_{rock,model}$ (kg m ⁻³)	3545	3545
	T_b (K)	250	255.70
	q_b mW m ⁻²	4	5
	q_c mW m ⁻²	16	18
	D_{Ih} (km)	130	100
	D_{ocean} (km)	20	132
	D_{III} (km)	46	-
	D_V (km)	120	79
	D_{VI} (km)	120	127
	R_{rock} (km)	1975	1973
	R_{core} (km)	617	598
	Water	ρ_{rock} (kg m ⁻³)	3500
$\rho_{rock,model}$ (kg m ⁻³)		3543	3543
T_b (K)		253.10	257.40
q_b mW m ⁻²		4	5
q_c mW m ⁻²		17	18
D_{Ih} (km)		120	100
D_{ocean} (km)		62	139
D_{III} (km)		16	-
D_V (km)		121	83
D_{VI} (km)		116	112
R_{rock} (km)		1975	1976
R_{core} (km)		623	624

Table 10. Callisto with $C/MR^2=0.32$ and anhydrous pyrolite composition. $Q_{rock} = 110$ GW

Table A.1. Ice Material Parameters

Crystalline Phase	D^b W m ⁻¹	ν^b Pa s	E^c kJ mol ⁻¹	K_S^d GPa	μ^d GPa
I	632	5×10^{13}	60	9.96	3.6
II	418	1×10^{18}	77	13.89	6.2
III	242	5×10^{12}	127	9.87	4.6
V	328	5×10^{14}	136	14.19	6.1
VI	183	5×10^{14}	110	18.14	7.5

^aadapted from *Andersson and Inaba* [2005] Table 1; ^b*Durham et al.* [2001] Table 4;

^c*Deschamps and Sotin* [2001]; ^d*Gagnon et al.* [1990]